

1 **Structural basis of PML/RARA oncoprotein targeting by arsenic unravels**
2 **a cysteine rheostat controlling PML body assembly and function**

3
4 **Authors & affiliations**

5 Pierre Bercier^{1,2#}, Qian Qian Wang^{3,4,5#}, Ning Zang^{4,8#}, Jie Zhang^{4,8}, Chang Yang^{3,4,5}, Yasen
6 Maimaitiyiming^{3,4,5}, Majdouline Abou-Ghali^{1,2}, Caroline Berthier¹, Chengchen Wu^{1,2}, Michiko
7 Niwa-Kawakita^{1,2}, Thassadite Dirami^{1,2}, Marie-Claude Geoffroy^{1,2}, Omar Ferhi^{1,2}, Samuel
8 Quentin², Shirine Benhenda², Yasumitsu Ogra⁶, Zoher Gueroui⁷, Chun Zhou^{*4,8}, Hua
9 Naranmandura^{*3,4}, Hugues De Thé^{*1,2,9} & Valérie Lallemand-Breitenbach^{*1,2}

10

11 ¹ Center for Interdisciplinary Research in Biology (CIRB), Collège de France, CNRS, INSERM, Université
12 PSL, Paris, France, ²GenCellDis, Inserm U944, CNRS UMR7212, Université Paris Cité, F-75010 Paris,
13 France ³Department of Hematology of First Affiliated Hospital, School of Medicine, Zhejiang
14 University, Hangzhou, China ⁴Public Health, School of Medicine, Zhejiang University, Department of
15 Toxicology, Hangzhou, China, ⁵College of Pharmaceutical Sciences, Zhejiang University, Hangzhou,
16 China, ⁶Graduate School of Pharmaceutical Sciences, Chiba University, 1-8-1 Inohana, Chuo, Chiba
17 260-8675, Japan, ⁷Department of Chemistry, École Normale Supérieure, PSL University, Sorbonne
18 Université, CNRS, ⁸Department of Pathology, Sir Run Run Shaw Hospital, Zhejiang University School
19 of Medicine, Hangzhou, China, ⁹Hematology Laboratory, Hôpital St Louis, AP/HP, Paris France

20

21 # Co-first authors * Co-senior and corresponding authors

22

23 **Running title:** Structural basis of PML/RARA targeting by arsenic

24 **Keywords:** PML Nuclear Bodies; Arsenic; Leukemia; B-Box; liquid-liquid phase separation

25

26 **Additional information**

27 Work in the Paris laboratories is supported by Collège de France, INSERM, CNRS, Université
28 Paris Cité), with financial support from ITMO Cancer of Aviesan within the framework of the
29 2021-2030 Cancer Control Strategy, on funds administered by Inserm (PCSI C22028DS, VLB;
30 22CP117, ZG), Fondation du Collège de France, European Research Council Advanced Grant
31 785917–PML-THERAPY, the Sjöberg Award (to H.d.T.), the last year of P.B.'s thesis was
32 funded by Fondation ARC pour la Recherche sur le Cancer (ARC). Work in Hangzhou is
33 supported by National Science Foundation of China (82170143 to H. N. and 31971125 to C.
34 Z.) and Zhejiang Innovation Team Grant (2020R01006).

35

36 **Chun Zhou**, Department of Pathology of Sir Run Run Shaw Hospital, and Department of
37 Public Health, Zhejiang University School of Medicine, Hangzhou, Zhejiang, China 310058.
38 Phone: +86 88208102 ; E-mail: chunzhou@zju.edu.cn

39 **Hua Naranmandura**, Professor, Department of Hematology of First Affiliated Hospital, and
40 Department of Public Health, Zhejiang University School of Medicine, Hangzhou, Zhejiang,
41 310058, China. Phone: +86 88206736; E-mail: narenman@zju.edu.cn

42 **Hugues de Thé**, Professor, Collège de France, Chair of Oncology, Center for Interdisciplinary
43 Research in Biology, U1050, Nuclear Organization and Post-Translational Control in Physio-
44 Pathology, Paris, France; Saint-Louis Research Institute, U944, Genomes and Cell Biology of
45 Diseases, Paris, France. Phone: +33 680667389 ; E-mail: hugues.dethe@inserm.fr

46 **Valérie Lallemand-Breitenbach**, Center for Interdisciplinary Research in Biology, Inserm
47 U1050 - CNRS UMR7241, Nuclear Organization and Post-Translational Control in Physio-

48 Pathology, 11 place Marcelin Berthelot, 75005 Paris, France. Phone: +33 611838602 ; E-mail:

49 valerie.lallemand@inserm.fr

50

51 HdT reports consulting fees for Syros Pharmaceuticals, Inc. (SYRS) unrelated to the topic of

52 this manuscript. There are no other conflicts of interest.

53

54 **Total number of figures:** 7 ; movies: 2 ; Supplementary Figures: 5

55 **ABSTRACT**

56 PML Nuclear Bodies (NBs) are disrupted in PML-RARA-driven acute promyelocytic leukemia
57 (APL). Arsenic trioxide (ATO) cures 70% APL patients, driving PML-RARA degradation and NB
58 reformation. In non-APL cells, arsenic binding onto PML also amplifies NB formation. Yet, the
59 actual molecular mechanism(s) involved remain(s) elusive. Here, we establish that PML NBs
60 display some features of liquid-liquid phase separation and that ATO induces a gel-like
61 transition. PML B-box-2 structure reveals an alpha helix driving B2 trimerization and
62 positioning a cysteine trio to form an ideal arsenic-binding pocket. Altering either of the
63 latter impedes ATO-driven NB-assembly, PML sumoylation and PML-RARA degradation,
64 mechanistically explaining clinical ATO-resistance. This B2 trimer and the C213 trio create an
65 oxidation-sensitive rheostat that controls PML NB assembly dynamics and downstream
66 signaling in both basal state and during stress response. These findings identify the structural
67 basis for arsenic targeting of PML which could pave the way to novel cancer drugs.

68

69 **50-word statement of significance**

70 Arsenic curative effects in acute promyelocytic leukemia relies on PML targeting. We report
71 a PML B-box-2 structure that drives trimer assembly, positioning a cysteine trio to form an
72 arsenic-binding pocket, mutated in resistant patients. Identification of this ROS-sensitive
73 triad controlling PML dynamics and function could yield novel drugs.

74 INTRODUCTION

75 ProMyelocytic Leukemia (PML) protein organizes the formation of stress-sensitive
76 membrane-less organelles (MLO): PML Nuclear Bodies (NBs). PML controls various biological
77 functions, such as apoptosis, senescence or stem cell self-renewal (1,2). PML may elicit these
78 functions by scaffolding the spherical shells of NBs, which subsequently act as hubs of post-
79 translational modifications, in particular sumoylation, for the broad range of proteins
80 trafficking through their inner cores. PML NBs are disrupted in Acute Promyelocytic
81 Leukemia (APL) driven by the PML-RARA oncogenic fusion protein. PML protein expression
82 and NB formation are also downregulated in many other cancers (3-5). The combination of
83 arsenic trioxide (ATO) and retinoic acid treatments drives APL cure by enforcing PML-RARA
84 degradation and PML NB re-assembly, subsequently leading to the activation of a
85 senescence-like program in APL cells (3). ATO, which as single therapy cures 70% of APL
86 patients (6,7), directly binds PML-RARA and PML proteins (8,9). While ATO-driven PML-RARA
87 degradation is biochemically well-understood (10), ATO-enforced NB-assembly remains
88 understudied. Formation of PML intermolecular disulfide bonds was reported in response to
89 ATO (8) and arsenic was proposed to replace a Zn^{2+} ion in the RING finger (9). However, ATO
90 effects on NB assembly remain imperfectly understood.

91 Biogenesis of MLO has been revisited through the prism of liquid-liquid phase
92 separation (LLPS). Biomolecular condensates may arise by multivalent weak interactions
93 between proteins, or proteins and RNAs, which de-mix from the surrounding media to form
94 spherical structures, maintained as an equilibrium despite dynamic exchange of their
95 components (11,12). LLPS has been proposed to increase kinetics of biochemical reactions
96 among its constituents and could contribute to diseases initiation (13,14). In leukemia,
97 chimeric transcription factors may condensate through LLPS, resulting in aberrant 3D

98 chromatin structures and contributing to their aberrant transcriptional activity (15,16). *In*
99 *vitro*, chimeric GFP-polySUMO proteins condense in droplets through LLPS when combined
100 with chimeric proteins containing repetitions of SUMO-Interacting motif (SIM) (17). Yet, PML
101 sumoylation is dispensable for PML NB assembly (18,19) and the contribution of LLPS in PML
102 NB assembly still remains elusive.

103 In this study, we elucidate the crystal structure of PML B-box 2 (B2) and identify an
104 α -helix that mediates B2 trimerization through hydrophobic interactions, controlling PML NB
105 assembly and PML dynamics. This α -helix-mediated trimer organizes a triad of free C213
106 cysteines to which trivalent arsenic covalently docks, switching PML NBs from liquid-like to
107 gel-like bodies. B2 trimerization and C213 are mandatory for PML-mediated function, such
108 as oxidative stress response *in vivo*, as well as ATO-triggered PML-RARA-degradation,
109 uncovering the very first step by which ATO achieves its anti-leukemia cure.

110

111 RESULTS

112 PML NBs switch from liquid-like to gel-like structures upon ATO

113 PML NBs are spherical membrane-less organelles forming core-shell structures (Fig.
114 1A). To determine whether PML assembly in NBs reflects liquid-liquid phase separation
115 (LLPS), we stably expressed GFP-PML-III in *Pml*^{-/-} mouse embryonic fibroblasts (MEFs) and
116 assessed hallmarks of liquid-like MLO: solubility limit, fusion/relaxation and dynamic
117 exchange. First, we examined whether PML could de-mix from the nucleoplasm above a
118 concentration threshold by live cell imaging following retroviral cell transduction. PML was
119 initially homogeneously distributed in the nucleoplasm, but as GFP-PML expression
120 increased, the first PML NB appeared (Fig. 1B) and NBs then became more numerous, while

121 the diffuse fraction remained constant (Supplementary Figure S1A). Similarly, the number of
122 PML NBs increases with PML transcriptional activation upon IFN alpha treatment (20,21).
123 Thus, PML de-mixes from a diffuse nucleoplasmic fraction into NBs above a concentration
124 threshold. Live cell imaging revealed that two PML NBs can fuse and relax in a novel single
125 spherical body, supporting liquid-like behavior of PML NBs (Fig. 1C and Supplementary
126 Movie 1). In these experiments, analysis of the relaxation curves, plotting the size of fusing
127 PML NBs as a function of time, allowed extraction of the diffusion coefficient of PML
128 proteins and a NB capillary viscosity of 10^3 Pa.s (Supplementary Figure S1B) (22), comparable
129 to that of nucleoli or nuclear speckles (23,24). We then quantified the number of events of
130 GFP-PML nucleation from the diffuse nucleoplasmic fraction, PML NB fusions or fissions (Fig.
131 1D). Fusion events occurrence were similar to nucleation ones, maintaining a mean number
132 of 40 PML NBs per nucleus, while fission events were rare. We then assessed the dynamics
133 of PML NB assembly by Fluorescence Recovery After Photobleaching (FRAP). As reported,
134 PML protein dynamically exchanges between the nucleoplasm and NBs, with a recovery $t_{1/2}$
135 of 3.2 min (Fig. 1E) (8,25,26). Taken together, these results establish that PML NBs exhibit
136 hallmarks of liquid-liquid phase separated condensates. However, the residence time of PML
137 at NBs is much longer than other MLO nucleators, such as those driving Cajal bodies,
138 speckles or nucleoli (minutes versus seconds), indicating higher affinity between PML
139 proteins at NBs. Moreover, 30% of the GFP-PML fluorescence bleached at NBs never
140 recovers (Fig. 1E), implying that two PML fractions coexist at NBs, one exchanging with the
141 surrounding nucleoplasm, the other remaining immobile. Together with the existence of the
142 core-shell structure, this challenges a pure LLPS of PML proteins as a simple model of NB
143 assembly.

144 ATO exposure rapidly increased PML NB-associated fraction at the expense of the
145 diffuse one and PML NB assembly dynamics dramatically dropped, so that almost all PML
146 became immobilized (Fig. 1E). Live-cell imaging and super-resolution microscopy showed
147 that PML NBs tend to aggregate without achieving complete fusion, forming PML NB strings,
148 consistent with an increase in the viscoelasticity (Figs. 1F-G and Supplementary Movie 2).
149 Thus, ATO triggers the transition from liquid-like to gel-like PML NBs.

150 PML fusion to RARA altered its distribution in the nucleus, as GFP-PML-RARA
151 localized into many tiny dots with diameter below 100 nm in *Pml*^{KO} MEFs (8,27) (Fig. 1G). The
152 basal dynamics of GFP-PML-RARA at these microdots was slightly increased compared to
153 PML at NBs, with a $t_{1/2}$ of 1.37 min and, importantly, no immobile fraction (Fig. 1H). Yet, here
154 again, ATO treatment decreased drastically PML-RARA exchange rates, closer to the
155 dynamics of PML. Thus ATO-therapy drives the gel-like transition of both PML- or PML-RARA-
156 driven condensates.

157

158 **PML NB assembly requires the B2-box domain rather than di-sulfide bridges**

159 Arsenic atoms may bind sulfhydryl groups, primarily targeting cysteine residues in
160 cells. Within PML, arsenic was proposed either to directly target cysteines of the RING finger,
161 in which arsenic would replace the structuring zinc atom, or the B-box 2 (B2), another zinc
162 finger domain which contains adjacent cysteines: C212 and C213 (8,9). We first assessed the
163 role of free cysteines in NB formation by using N-ethyl-maleimide (NEM), which alkylates
164 cysteine residues with a freely accessible -SH group. Pre-treatment with NEM blocked both
165 basal PML NB-assembly and ATO-enforced PML NB formation (Fig. 2A). Conversely,
166 treatment with ATO precluded subsequent NEM-induced disorganization of PML NBs. Thus,
167 the cysteine(s) required for baseline NB assembly are accessible, not involved in zinc

168 coordination and likely the same as those targeted by ATO. This does not support the RING
169 finger as being the primary ATO target site.

170 ATO exposure induces ROS production due to GSH scavenging and mitochondrial
171 poisoning (28-30). We previously showed that disulfide bonds may link PML monomers,
172 driving their covalent multimerization upon oxidative stress (8). We sought to disentangle
173 the respective contribution of direct arsenic binding or ATO-enhanced disulfide bonds in
174 PML NB assembly. By homology with other TRIM proteins, the C213 residue is likely not
175 involved in zinc coordination (31). We thus focused on both C213 and C389, the latter being
176 an oxidation-sensitive residue implicated in oncoprotein targeting (32,33). PML
177 intermolecular disulfide bonds can be assessed by Western blot analysis in non-reducing
178 conditions, which revealed high molecular weight PML multimers, whose abundance sharply
179 increased upon ATO or H₂O₂ (Fig. 2B, Supplementary Figure S1C) (8), but were lost under
180 reducing conditions (Supplementary Figure S1C,D). C389S mutation impaired ATO-induced
181 disulfides, but only modestly affected those induced by H₂O₂, while C213A decreased PML
182 intermolecular bound species induced by both ATO and H₂O₂. The double C213A/C389S
183 mutation completely abrogated the formation of these PML multimers (Fig. 2B).

184 Following PML NB assembly, PML becomes sumoylated (18,21,34). ATO-induced
185 gel-like NBs are associated with a massive increase in PML sumoylation (Fig. 2B).
186 Interestingly, PML^{C213A} mutants were defective for sumoylation, while PML^{C389S} did not affect
187 basal or ATO-induced SUMO conjugation of PML. We then assessed the localization patterns
188 of wildtype or mutant PML upon those stress. Surprisingly, in contrast to ATO, H₂O₂ did not
189 significantly alter the diffuse nuclear fraction of WT PML, nor increase the NB-associated
190 fraction, suggesting that intermolecular disulfides are not responsible for gel-like transition
191 (Fig. 2C). Critically, C213A or C389S mutations had very different effects on NB formation

192 (Fig. 2C). While defective for ATO-induced disulfide, PML^{C389S} NBs and diffuse fraction were
193 identical to those of WT PML, including full ATO sensitivity. In contrast, PML^{C213A} remained
194 mainly diffuse, with a single enlarged body, unaffected by ATO. Taken together, these results
195 indicate that C213 is essential for PML NB assembly, but intermolecular disulfide bonds
196 mediated by C213 or C389 are not, and suggest that C213 may directly contribute to arsenic
197 binding.

198

199 **Crystal structure of PML B2 box reveals an α -helix exposing C213**

200 B-box domains are found in TRIM (TRIPartite Motif) proteins and are often involved
201 in protein-protein interaction (31). We identified a highly conserved short sequence
202 encompassing the adjacent cysteines C212/C213 in all PML-like proteins across evolution
203 (Fig. 3A). Interestingly, this stretch of conserved residues exactly corresponds to the hotspot
204 mutations of PML-RARA or PML in therapy-resistant APL patients (35-38).

205 Despite numerous attempts, no PML B2 crystal structure has been reported to date.
206 We fused MBP to PML B2 to produce a soluble fusion protein from bacteria, and obtain a
207 crystal structure at 2.1 Å resolution (Fig. 3B, Supplementary Figure S2A). In this structure, B2
208 domain adopted a typical B-box-type zinc finger fold, where C3H1 residues coordinated two
209 zinc atoms in a cross-braced conformation and with a conserved β 1- β 2- α 1 arrangement
210 (Figs. 3B-C). Analysis of the crystal packing showed that B2 was sandwiched between two
211 MBP molecules. Indeed, B2 β 1 formed an anti-parallel β sheet with MBP β 8 through main
212 chain hydrogen bonds, while B2 α 1 packed against a hydrophobic patch in the neighboring
213 MBPs (Supplementary Figures S2A-C). Structure alignment demonstrated that PML B2 was
214 similar to other TRIM family B2 domains, such as TRIM5 or TRIM28, although PML B2
215 appears to be more flexible with longer loops (Supplementary Figures S2D-G) (39,40). In the

216 first zinc finger, zinc coordination involved C212, but importantly, not C213, which was
217 positioned at the edge of the α 1-helix pointing out of the overall B2 structure (Figs. 3B and
218 C). Remarkably, this helix corresponds to the evolutionary conserved primary sequence
219 identified above (Fig. 3A, Supplementary Figures S2D and S2F). In the second zinc finger, the
220 zinc was coordinated by C227 instead of the AlphaFold-predicted D219 (Fig. 3B and
221 Supplementary Figures S2D-E). Note that C227 is not conserved in TRIM5 or TRIM28 B2 nor
222 are the residues from the conserved α helix (Supplementary Figures S2D-G). The residues
223 equivalent to PML C227-surrounding sequence in TRIM5 and TRIM28 form a β 3 strand - that
224 does not coordinate zinc (Supplementary Figures S2D and F-G). Altogether, we have
225 unraveled the PML B2 structure, highlighting an α -helix that positions outwards the free
226 C213 that is key to NB assembly.

227

228 **PML B2 α 1-helix and C213 drive NB assembly and dynamics**

229 To determine the respective roles of PML B2 zinc fingers and the C213-containing
230 helix in NB assembly, we engineered mutations disrupting zinc coordination (C189S or
231 C212S) or point mutations on the α 1-helix (C213S or L218G) and stably expressed these GFP-
232 tagged PML mutants in *Pml*^{KO} MEFs. All these PML mutants exhibited a sharply increased
233 nuclear diffuse fraction with only one to three unusually large bodies, implying that this α 1-
234 helix and C213 play key roles in NB formation (Fig. 4A, supplementary Figure S3A).

235 FRAP analysis showed a slight increase in the GFP-PML^{C189S}, GFP-PML^{C212S} or GFP-
236 PML^{C213S} body assembly dynamics, with similar immobile fractions when compared to WT
237 PML (Figs. 4B,C, Supplementary Figure S3B). In contrast, C213S or L218G mutations
238 drastically increased the dynamics of PML NB assembly, with a drop of the half recovery time
239 from 3.2 min to 0.6 or 0.8 min respectively. Moreover, we observed a complete recovery of

240 the photobleached C213S and L218G PML proteins at the remaining body, pointing to a fully
241 liquid compartment. Thus, the α 1-helix, including C213, dictates PML dynamics and NB
242 assembly. The crystal structure of MBP-PML B2 with C213A and A216V double mutation
243 (A216V being the hotspot mutation in ATO resistance (35,36)) was very similar to that of WT
244 B2, with an RMSD of 0.26 Å over 42 C α atoms (Fig. 4D and Supplementary Figure S3C). This
245 supports the idea that the effects of these α 1-helix mutations on PML NB assembly dynamics
246 were not due to B2 folding alterations, but rather to loss of its biochemical interactions.
247 Overall, while the zinc fingers contribute to the overall domain structure, the conserved α 1-
248 helix is crucial for PML NB assembly and dynamics.

249

250 **Alpha-helix mediated hydrophobic B2 trimerization is key for NB dynamics**

251 TRIM5 α B2 was proposed to trimerize through a specific α -helix around a
252 tryptophan core *in vitro* (39). We thus looked whether PML B2 monomers could self-
253 assemble into a trimer through Alphafold2 molecular modeling (Fig. 5A, B). In the model, the
254 trimer is predicted to be driven by α 1-helix mediated interactions, involving hydrophobic
255 interfaces and in particular, I202, C213, A216, L217 and L218 (Fig. 5A). More specifically,
256 L217 is predicted to play a very central role through its two methyl groups, each bridging two
257 other PML B2 monomer through their own L217, as well as with one I202 on β 1 (Fig. 5B).
258 Interestingly, L218 could also interact with I202 of another PML B2, further securing this B2
259 complex (Fig. 5B). Supporting B2 trimerization *in vitro*, SEC-MALS analysis revealed three
260 forms of purified MBP-B2 with molecular weights corresponding to monomer, dimer and,
261 critically, abundant trimer (Fig. 5C).

262 To interrogate the relevance of this model *in cellulo*, we generated point mutations
263 of these potentially interfacing residues. When analyzed by immunofluorescence, L217G

264 substitution had the most drastic effect, completely blocking PML NB assembly (Figs. 5D,
265 quantification in Supplementary Figure S3A). GFP-PML^{I202A} or GFP-PML^{L218G} localization were
266 diffuse in the majority of cells and formed one or two bodies in the remaining ones. A similar
267 defect in NB assembly was observed with the A216V patient-derived mutation (35-37),
268 consistent with our model predicting a constraint environment due to the short distance
269 between A216 and L217 side chain within the trimer (Figs. 5B, 5D). In contrast, the A216G
270 mutation had only minor effects, increasing the diffuse PML fraction, consistent with its
271 predicted modest impairment of trimerization. When analyzed in FRAP, PML^{I202A}, PML^{A216V},
272 or PML^{L218G}, all exhibited highly dynamic exchange with liquid-like behaviors (Fig. 4B,
273 Supplementary Figure S3B). Conversely, increasing hydrophobicity by substituting leucine to
274 residues with aromatic group at position 218 led to the formation of filaments, on which
275 PML exchange was poorly dynamic (Fig. 5E and Supplementary Figures S3D-E). Thus, the α 1-
276 helix-mediated hydrophobic interactions between PML monomers through I202, L217 and
277 L218 regulate PML assembly ranging from large liquid-like bodies, standard PML NBs to gel-
278 like filaments.

279

280 **Arsenic docks on a C213 tri-cysteine pocket of B2 trimers to drive gel-like** 281 **transition**

282 In APL, ATO and other therapeutic arsenic derivatives provide trivalent arsenic
283 (As(III) oxidation state) at physiological pH and *in vivo*. As(III) can form stable complexes with
284 thiol groups through covalent binding to sulfur and may form complex with three
285 glutathiones in solution (30). Critically, the key C213 residues are organized in a triad
286 positioned at the center of the PML B2 helix trimer (Fig. 6A, supplementary Figures S4A,B), in
287 an enzymatic active center-like configuration. This triad is present at the opposite end of the

288 assembled helices compared to the sites of L217 interactions (Fig. 5B, Fig. 6A). The C213
289 residues are separated by 3.2 Å, fitting with an ideal arsenic docking that would lead to an
290 interacting distance of 2.7 Å between arsenic and the sulfur atoms (Fig. 6A, supplementary
291 Figures S4A-B). We thus hypothesized that ATO could trigger gel-like transition of PML NBs
292 by targeting this triad of C213 residues within the B2 trimer. We first tested whether the
293 effect of ATO on PML NBs depends on arsenic valency. We used monomethyl arsenic
294 (MMA), which may only bind 2 cysteines, as well as antimony (Sb) trioxide (STO) that
295 releases trivalent Sb, the closest chemical to As(III). In contrast to ATO, MMA has no effect
296 on the dynamics of PML NB assembly (Fig. 6B) (41). Conversely, STO had very similar effects
297 to ATO, decreasing the PML diffuse fraction, turning PML NBs in gel-like string bodies (Fig.
298 6B, Supplementary Figure S4C) and subsequently increasing PML sumoylation
299 (Supplementary Figure S4D) (42).

300 For B2 mutants of zinc finger 1 formation (C212S, C189S), or mutants impairing
301 helix-driven trimerization, as well as for C213S, PML nuclear distribution was unaffected by
302 ATO treatment (Fig. 6C). ATO could not drive phase transition of C213S or helix trimer
303 mutant-forming bodies, as supported by FRAP analyses (Fig. 6D, Supplementary Figure S4E).
304 In contrast, A216G mutation only marginally affected ATO-response of PML, as expected
305 from our model (Fig. 6C-D). ReAsH - an arsenic derivative that fluoresces when bound to
306 proteins - labelled the GFP-PML shell and triggered gel-like transition of PML NBs, similar to
307 ATO (Fig. 6E) (8). In contrast, the shell of the body formed by PML^{C213S} could not bind ReAsH.
308 Rather, ReAsH accumulated within the NB inner core, an unexpected observation that
309 deserves further studies. Similarly, PML^{L218G} failed to bind ReAsH, stressing the fact that
310 efficient arsenic binding depends on both C213 and α 1-helix trimerization. Finally, the effect
311 of ATO on PML NBs after 30min-exposure was not reversed by washout experiments after

312 removing ATO, suggestive for covalent binding (Supplementary Figure S4F). Altogether our
313 findings imply that As(III) requires prior B2 helix trimerization to directly and irreversibly
314 targets C213 and trigger gel-like transition.

315 While mutations of C213 removing thiol group (C213S or C213A) and increasing
316 steric hindrance (C213L or C213F) all disrupted basal PML NB assembly, replacing C213 by
317 valine unexpectedly fully rescued the basal NB formation and normal dynamics (Figs. 6D,F).
318 These data suggest that the branched methyl groups of three valines can maintain
319 hydrophobic interactions within the center of the B2 trimer, somehow similar to L217 on the
320 other side of the helix. Strikingly, both PML C213V localization and dynamics were
321 insensitive to ATO, implying that the sensor function was lost (Figs. 6C,D). Accordingly,
322 alkylation by NEM, which disrupted WT NBs, had no effect on PML^{C213V} NBs (Figs. 2A and
323 6G), stressing the unique features of this cysteine residue. Altogether, this suggests that,
324 within the B2 domain, C213 thiol modification controls PML NB assembly dynamics.

325 Basal PML sumoylation was severely impaired in all mutants predicted to destabilize
326 the B2 trimer and alter NB formation (Fig. 6H,I). In contrast, basal PML^{C213V} sumoylation was
327 normal or even enhanced (Fig. 6I), while critically, sumoylation of PML^{C213V} was ATO-
328 insensitive (Fig. 6I, Supplementary Figure S4G,H). As expected, all B2 trimer and other C213
329 mutants were resistant to ATO-enhanced sumoylation. PML sumoylation of K160 drives
330 partner recruitment (18,43). Accordingly, PML^{C213V} efficiently recruited partner proteins,
331 such as Sp100 (Fig. 6J) and the RNF4 SUMO-dependent ubiquitin ligase (Supplementary
332 Figure S4I), while PML^{C213S} did not. As expected, in contrast to PML, ATO did not further
333 promote recruitment of partners into C213V bodies (Fig. 6J). Accordingly, all B2 mutant were
334 resistant to ATO-induced SUMO-triggered degradation (Fig. 6I, Supplementary Figures

335 S4G,H). Thus, C213-mediated trimerization controls PML sumoylation and partner
336 recruitment.

337 PML NBs couple oxidative stress to control of partner sumoylation through
338 recruitment of UBC9 (18,21). We questioned whether impeding α 1-mediated B2
339 trimerization would affect partner biochemical modifications. We generated a *Pml*^{L222G} mESC
340 line (corresponding to L218G in human PML forming liquid-like bodies), stably expressed
341 His₁₀-SUMO2 and we purified SUMO2 conjugates before or after ATO exposure. As we
342 previously described (21), ATO enhanced global sumoylation, as well as that of endogenous
343 mouse PML (mPML) and KAP1 (Fig. 6K). None of these were observed in *Pml*^{L222G} mESC (Fig.
344 6K, Supplementary Figure S4J). Thus, α 1-mediated B2 trimerization is required for the
345 biochemical function of PML NBs to promote partner sumoylation.

346

347 **C213 mediates PML-RARA ATO-sensitivity**

348 We then assessed the role of PML C213 residue in the context of the oncogenic
349 PML-RARA protein, by transducing hematopoietic progenitors (HSPCs) and MEFs with WT or
350 C213 mutant PML-RARA. We first examined the distribution of human PML-RARA and
351 endogenous mouse Pml proteins by immunofluorescence. As previously shown (27,44),
352 PML-RARA exhibited a micro-speckled pattern where it recruited endogenous mPML. In
353 contrast, PML-RARA^{C213S} was diffuse in the nucleus, consistently with C213 role in PML-RARA
354 assemblies, but endogenous mPML NB formation was unaffected in both MEFs (Fig. 7A) and
355 HSPCs (Supplementary Figure S5A). PML-RARA^{C213V} formed numerous small microdots and
356 also disrupted endogenous mPML localization, similar to PML-RARA^{WT}. Thus, C213 controls
357 the efficiency of homo- and hetero-interactions between PML-RARA and Pml within micro-
358 speckles. In ATO-treated primary progenitors or MEFs, PML-RARA and mPML progressively

359 reassembled into NBs (Fig. 7A, Supplementary Figure S5A). In sharp contrast, PML-RARA^{C213S}
360 did not respond to ATO, while endogenous mPML aggregated into fewer NBs (Fig. 7A,
361 Supplementary Figure S5A). Finally, PML-RARA^{C213V}-expressing cells had a mixed phenotype,
362 with ATO-aggregated endogenous mPML NBs - particularly in progenitors that express high
363 levels of mPML proteins, but unresponsive PML-RARA micro-speckles. We then examined
364 the effects of ATO on PML-RARA sumoylation/degradation (45). In the context of the
365 oncogenic protein, C213S precluded basal PML-RARA sumoylation, while PML-RARA or PML-
366 RARA^{C213V} were both efficiently sumoylated in the basal state (Fig. 7B). Importantly, the two
367 C213 mutants were completely resistant to ATO-triggered hyper-sumoylation and
368 degradation (Fig. 7B quantification in Supplementary Figure S5B), explaining the remaining
369 PML-RARA^{C213V} micro-speckles (Fig. 7A, Supplementary Figure S5A). In FRAP analyses
370 performed either in *Pml* proficient (Supplementary Figures S5C,D) or null MEFs (Fig. 7C),
371 PML-RARA^{C213V} mutation reduced the basal assembly dynamics of PML-RARA microdots, but
372 blocked ATO-driven gel-like transition, consistent with its inability to bind arsenic.
373 Altogether, these data demonstrate the key role of C213 in ATO-targeted effects on PML and
374 PML/RARA. Interestingly, dynamics of PML-RARA were distinct in *Pml* proficient or null
375 background (Fig. 7C, Supplementary Figure S5C), supporting that PML reduces PML-RARA
376 assembly dynamics and could contribute to its ATO sensitivity.

377

378 **B2 trimer and C213 control oxidative stress responses**

379 The role of PML is likely much broader than being just an arsenic binder and PML
380 was repeatedly linked to oxidative stress (46-49). To question any contribution of the C213
381 triad in oxidative stress sensing, we compared the effects of ROS on PML NB assembly
382 dynamics in PML and PML^{C213V}. Depending on the dose, H₂O₂ increased or decreased PML

383 dynamics assessed by FRAP (Fig. 7D). Remarkably, PML^{C213V} was completely insensitive to
384 H₂O₂ (Fig. 7E), suggesting that C213 modification by ROS regulates NB dynamics and could
385 play an important role in oxidative stress-sensing.

386 PML is involved in oxidative stress responses (50,51), notably in hepatocytes (46).
387 To explore any role of B2 trimerization, we engineered a *Pml*^{A220V} knock-in mice
388 (corresponding to the A216V hotspot mutation in the human sequence). Similar to *Pml*^{-/-}
389 mice, these animals did not exhibit obvious phenotypes and were fertile. As for stably
390 expressed PML^{A216V} mutant (Fig. 5D), rare mPML^{A220V} nuclear bodies were observed in
391 hepatocytes and the mutant protein did not undergo detectable sumoylation
392 (Supplementary Figure S5E). Hepatocytes from *Pml*^{A220V} or *Pml*^{-/-} animal exhibited an
393 increased number of γ H2AX foci (Fig. 7F), which could reflect basal oxidative stress (46) or
394 defects in DNA-repair (52). Transcriptomic studies and GSEA analyses comparing basal gene
395 expression in the livers of *Pml*^{A220V} and WT animals revealed major differences (including
396 stress signatures, Fig. 7G), many of which were shared with *Pml*^{-/-} animals (Supplementary
397 Figure S5F). Thus, B2 trimer formation has important consequences in physiological
398 conditions.

399 We then subjected WT, *Pml*^{A220V} and *Pml*^{-/-} animals to CCl₄, a classic trigger of
400 oxidative stress, ultimately resulting in fibrotic scars, which are limited by senescence
401 activation (53). We first examined acute response by performing transcriptomic studies of
402 livers 18h post-injection. Remarkably, differentially regulated pathways compared to WT
403 animals were virtually identical between *Pml*^{A220V} and *Pml*^{-/-} ones (Fig. 7H), highlighting
404 defects in multiple pathways, including p53, E2F, G2M checkpoint, fatty acid, hypoxia, IFNs,
405 Myc, TNF α or TGF β . They are functionally related to processes regulated by PML, such as
406 apoptosis and senescence, cell growth, metabolism, oxidative stress response, as well as

407 inflammatory processes (1,2,50). When we examined liver fibrosis after 5 weeks of
408 treatment, increased fibrosis was noted upon Picro-Sirius red staining in *Pml*^{A220V} and *Pml*^{-/-}
409 animals when compared to WT controls (Fig. 7I), as expected from impaired P53 activation
410 and senescence (53).

411 Altogether our findings support that B2 helix-positioned C213 triads act as rheostats
412 controlling PML NB assembly dynamics, liquid- to gel-like properties, and sumoylation,
413 depending on C213 oxidation states (Fig. 7J). This rheostat controls physiological functions of
414 PML for basal homeostasis and stress adaptation. As(III) highjacks this sensor, turning
415 reversible interactions into high-affinity ones, ultimately driving PML-RARA
416 sumoylation/degradation and yielding APL cure.

417

418 **DISCUSSION**

419 In this study, based on the first determination of PML B2-box crystal structure, we
420 unravel the PML/arsenic interplay on a cysteine trio within a B2 trimer, driving a
421 polymerization-like process of PML NB assembly.

422 Despite repeated claims, there was little available experimental evidence that PML
423 undergoes phase separation. Here, we show that PML can de-mix from the nucleoplasm,
424 forming bodies as a result of a dynamic process of PML exchange between condense and
425 diffuse fractions, with viscosity similar to other LLPS-driven NBs. PML NB biogenesis and LLPS
426 were proposed to rely on SUMOs and SUMO-interacting motifs (17,54). Yet, PML mutants on
427 sumoylation sites can nevertheless de-mix into few bodies, underscoring the dispensable
428 nature of sumoylation for PML condensation (18,19). Our FRAP data unravels that the typical
429 PML NB assembly dynamics is the result of complex PML self-interactions requiring B2
430 trimers rather than a “pure” multi-SUMO/SIM-driven LLPS. PML crystal structure and B2

431 trimer model resembles that of TRIM5 α (39), with PML-specific tunable central cysteine
432 residues that set PML NB assembly dynamics. Since liquid-like bodies are defective for PML
433 and partner sumoylation, while ATO-induced gel-like condensates promote both of them, we
434 have unraveled tight links between NB biochemical activity and B2-controlled PML NBs
435 dynamics.

436 Arsenic may bind three adjacent cysteines on the same polypeptide (55,56). Here,
437 arsenic binding is achieved through a trio of C213 residues from distinct B2 polypeptides,
438 locking a polymeric-like PML complex and driving gel-like transition. *In vivo*, interfering with
439 C213 positioning, with the mouse equivalent of the A216V mutation, induced basal and
440 stress-responsive transcriptional changes similar to those observed in *Pml*^{-/-} cells (47). These
441 included defects in p53, E2F, fatty acid metabolism, hypoxia, Myc, TNF α or TGF β (Fig. 7H),
442 many of which are directly implicated in oxidative stress response and altered in cancers.
443 Thus, in physiological conditions, the oxidation status of the sulfur atoms of C213 trio could
444 be the rheostat of NB biogenesis, accounting for their oxidative stress sensitivity (46,48,51).
445 The biochemical nature of oxidation status changes in the C213 triad remains to be
446 investigated. Distinct from C213, C389-mediated oxidation or disulfide formation may be
447 involved in other functions (33), such as ROS buffering within NBs (21).

448 ATO drives APL remission through PML-RARA degradation and subsequent PML NB
449 reformation (3,57). PML-RARA^{C213S} lost the ability to form micro-speckles and delocalize
450 endogenous mouse PML. In this setting, mPML localization was normal and remained fully
451 ATO-sensitive. A similar situation may be observed during clinical resistance observed in
452 PML-RARA B2-mutated APL patients (36,37). Thus, although ATO-induced NB-restoration is
453 required in murine APL models (57), it may be insufficient to initiate response, without

454 concomitant degradation of PML-RARA and the resulting clearance of master genes
455 promoters (58).

456 Identification of the 3D catalytic-like site controlling NB assembly could allow the
457 design of novel arsenic-like molecules to enhance or impede NB formation. These could be
458 of high value for PML NB-targeted therapies (59), or conversely, in cancers where PML is an
459 important survival factor (60,61). Overall, our results elucidate the long-standing question of
460 ATO targeting of PML (62,63) and unravel novel basic regulatory mechanisms which are
461 likely to be important in other physio-pathological settings.

462

463 **Acknowledgements**

464 We acknowledge the Orion technical core, CIRB (Tristan Pilot), for their support on
465 STED analysis (Julien Dumont), and the image analysis on QuPath (Gaëlle Letort, Héloïse
466 Monnet, Philippe Maily), as well as the histology core facility (Estelle Anceaume), and
467 Magali Fradet for cell sorting support. We thank the UMS Saint Louis US53 / UAR2030,
468 Université Paris Cité - INSERM - CNRS, Institut de Recherche Saint-Louis (Niclas Setterblad)
469 for the microarray analysis, and the zootechnicians and Véronique Parietti for taking care of
470 animal models on the "Plateforme d'investigation pré-clinique". We thank the staff at SSRF
471 BL19U1 for X-ray diffraction data collection and the staff at the National Facility for Protein
472 Science in Shanghai (NFPS) for their help with SEC-MALS experiments.

473 We thank our funding supports, INSERM, CNRS and Collège de France (H.d.T. and V.L.B.),
474 Université Paris Cité (H.d.T.) ITMO Cancer of Aviesan within the framework of the 2021-2030
475 Cancer Control Strategy, on funds administered by Inserm (PCSI C22028DS, VLB; 22CP117,
476 ZG), Fondation du Collège de France, European Research Council Advanced Grant 785917–
477 PML-THERAPY, the Sjöberg Award (H.d.T.), Fondation ARC pour la Recherche sur le Cancer

478 (ARC). National Science Foundation of China (82170143 to H. N. and 31971125 to C. Z.) and
479 Zhejiang Innovation Team Grant (2020R01006 to H.N.).

480

481 **Authors contributions**

482 PB, QQW and NZ performed all experiments; PB and QQW performed cell biology
483 experiments and generated PML mutations, PB performed live cell imaging, FRAP analyses
484 and transcript extraction from liver. NZ and JZ expressed, purified and crystallized MBP-B2
485 fusion proteins, CZ determined the structures. CW generated the first live cell imaging as
486 well as the PML C389S and C213/389S WB and IF analyses; MAG, CB and MCG provided the
487 data on PML-RARA (WT and mutants generated by PB) in Lin⁻ progenitors and MEFs and PML
488 partner recruitment. JZ performed SEC-MALS experiments, MNK generated and
489 characterized the *Pml*^{A220V} knock-in mouse and initiated the CCl₄ experiments, which were
490 developed by TD, S.Q. analyzed transcriptomics data and SB initiated C213S and C389S
491 mutants and observations on their defects. ZG computed PML NB viscosity. CZ, HN, HdT and
492 VLB designed experiments, interpreted data, with the active contribution of PB, QQW, NZ,
493 who performed critical readings of the manuscript. PB assembled the figures. CZ and HN
494 extensively discussed with VLB and HdT who wrote the paper, which was reviewed and
495 accepted by all co-authors.

496

497 **METHODS**

498 **Sequence analysis, cloning and constructs**

499 Human PML B2 amino acid sequence was extracted from the NCBI databank
500 (NP_150241.2) and compared to the following sequences: *Macaca mulatta*

501 (NP_001035899.1), *Mus musculus* (NP_835188.2), *Molossus molossus* (XP_036113734.1),
502 *Gallus gallus* (XP_004943755.1), *Chrysemys picta bellii* (XP_042707508.1). Amino acid
503 conservation was assessed using the ClustalW2 software (64).

504 PML mutations were performed in pMSCVpuro-HA-PMLIII or pMSCVpuro-GFP-
505 PMLIII using the Q5 site-directed mutagenesis kit (NEB; Cat. n°E0554S) according to the
506 manufacturer's protocol and controlled by sequencing (Eurofins Genomics). PML-RARA was
507 cloned into pMSCVpuro (SfiI/Agel) from pMSCVpuro-GFP-PMLIII and pMSCV-PML-RARA-neo.
508 PML-RARA B2 mutants were generated using AvrII/SfiI restriction fragments from
509 pMSCVpuro-GFP-PMLIII mutants. Restriction enzymes and T4 DNA ligase were purchased
510 from NEB. Additional primer sequences used for site-directed mutagenesis can be found in
511 Supplementary table S1.

512 **Cell culture and cell treatments**

513 All reagents and cell sources are indicated in Supplementary tables S2,S3. Large T-
514 transformed *Pml^{KO}* MEF cells (our laboratory (46)), HEK293T (Platinum-E from Catherine
515 Lavau, Durham, USA), and HeLa cell lines were maintained in DMEM (Thermo Fisher
516 Scientific; Cat. n°41966029) supplemented with 10% Fetal Calf Serum (FCS), 50U/ml
517 penicillin/streptomycin (Thermo Fisher Scientific; Cat n°10378016), 2mM glutamine (Thermo
518 Fisher Scientific; Cat n°25030024), at 37°C with 5% CO₂. *Pml^{WT}* mESC were originally
519 obtained from P. Navarro (Pasteur Institute, Paris, France) and cultured in the same culture
520 medium as MEFs, supplemented with 1% non-essential amino acid (Thermo Fisher Scientific;
521 Cat n°11140050), 1% Glutamax (Thermo Fisher Scientific; Cat n°35050-038), 1000 units/ml of
522 recombinant Leukemia Inhibitory Factor (LIF, Sigma-Aldrich; Cat n°ESG1107) and 0.1% β-
523 mercaptoethanol (Merck; Cat n°M6250) on gelatin-coated plates. Hematopoietic stem and
524 progenitor cells isolation, culture and transformation with PML-RARA were performed as

525 described before (65). *Pml*^{KO} MEFs were transduced using retroviruses produced by
526 Platinum-E packaging cells, after transfection with Effectene reagent (Qiagen; Cat. n°. 301425) with pMSCVpuro-HA-PMLIII or pMSCVpuro-GFP-PMLIII WT or mutants. GFP-positive
527 cells were sorted by flow cytometry (Aria II BD-Bioscience) or selected using 2µg/ml
528 puromycin (Sigma-Aldrich; Cat. n°P8833). HeLa-PML^{L218Y} cell line was generated by retroviral
529 transduction. pLVX-CMV-GFP-PMLIII L218Y retroviruses were generated by co-transfection
530 into HEK293T cells as above. For colocalization studies between PML and RNF4 or Sp100,
531 Platinum-E cells were transfected with both pMSCVpuro-GFP-PMLIII WT or mutant and
532 pMSCV-Sp100 or pMSCV-Flag-RNF4 and the culture supernatant was used to transduce
533 *Pml*^{KO} transformed MEFs. All cell lines used were negative for mycoplasma (monthly tested
534 by Eurofins MWG France) and were manipulated separately to avoid any cross
535 contamination during cell passages. The different stable cell lines were at least monthly
536 checked for authentication, based on human or mouse PML expression, sumoylation status
537 and subcellular distribution by immunofluorescence and Western blot analyses. They were
538 frozen before the third passage and kept for 10 to 20 passages, except for PML/RARA-
539 transduced MEFs or progenitors were less than 5 passages. No karyotype was performed,
540 except for knock in mESCs (see below).

542 Cells were treated with 1µM As2O3 (Sigma-Aldrich; Cat. n° 01969), 10µM N-ethyl-
543 maleimide (Sigma-Aldrich; Cat. n°E3876), 100 or 500µM H₂O₂ (Sigma-Aldrich; Cat. n°516813),
544 2µM Methylarsonic acid (Greyhouse; Cat. n°N-12922), 2µM cacodylic acid (Sigma-Aldrich;
545 Cat. n°C0125), 1µM antimony oxide (Sigma-Aldrich; Cat. n°637173-100G) or 2µM ReAsH
546 (Thermo Fisher; Cat. n° T34562).

547 **Western blot analysis**

548 Cell extracts were obtained using homemade Laemmli buffer devoid of reducing
549 reagents (200mM Tris pH 6,8, 8% SDS, 40% glycerol, 0,2% bromophenol blue), supplemented
550 with 20mM N-ethyl-maleimide (Sigma-Aldrich; Cat. n°E3876) for Western blot analysis in
551 non-reducing conditions, or supplemented with 50mM TCEP, or using direct lysis in
552 commercial Laemmli buffer (Sigma-Aldrich; Cat. n° S3401). SDS-PAGE analyses were
553 performed with 4-12% NuPAGE bis-tris gels (Thermo Fisher, Cat. n°NP0336) and
554 immunoblotted on nitrocellulose membranes (BioTrace Pall Laboratory; Cat. n°732-3031),
555 with antibodies: anti-GFP (1/1000, Roche; Cat. n°11814460001), anti-HA (1/1000, Covance;
556 Cat. n°MMS-101R-1000), anti-Actin (1/1000; Sigma-Aldrich; Cat. n°A2066), homemade anti-
557 hPML. Secondary antibodies from Jackson Immuno-Research: anti-Mouse-HRP (1/5000, Cat.
558 n°115-035-062), anti-Rabbit-HRP (1/5000, Cat. n°111-035-045). Proteins were detected using
559 SuperSignal West Dura or Femto (ThermoFisher; Cat. n°34076 and 34096), using Vilber
560 Fusion-Fx (Vilber). To avoid non-specific signals, membranes were not reprobed.

561 **Immunolabelling and microscopy analysis**

562 Cells were fixed with formalin 10% (Sigma-Aldrich; Cat. n°HT501128) for 15 min and
563 permeabilized in PBS 0.5% Triton x-100 (Sigma-Aldrich; Cat. n°T9284) for 15 min. Incubation
564 with antibodies was performed in PBS 0.5% Triton X-100 for 1h. Primary antibodies: anti-GFP
565 (1/1000, Roche; Cat. n°11814460001), anti-HA (1/1000, Covance; Cat. n°MMS-101R-1000),
566 anti-FLAG (11000, Sigma-Aldrich; Cat. n°F7425), homemade anti-hSP100 antibody,
567 homemade anti-hPML and anti-mPML antibodies, anti-SUMO2/3 (1/500, Cell Signaling
568 Technologies; Cat. n° 4971P), γ H2AX (Cell Signaling Technologies; Cat n°2577S). Secondary
569 antibodies: goat anti-mouse Alexa Fluor 488 (1/500, Jackson Immuno-Research; RRID:
570 AB_2338840), goat anti-mouse rhodamine red-X (1/500, Jackson Immuno-Research; RRID:
571 AB_2338756), goat anti-rabbit Alexa Fluor 488 (1/500, Jackson Immuno-Research; RRID:

572 AB_2338046), goat anti-mouse rhodamine red-X (1/500, Jackson Immuno-Research; RRID:
573 AB_2338022). Secondary goat anti-mouse antibody (STAR RED (1/250, Abberior; Cat. n°
574 STRED-1001) was used for STED analysis. DAPI (1µg/mL) from Thermo Fisher (Cat. n° 62248).
575 Image acquisitions were performed using a confocal microscope LSM 980 (Carl Zeiss Micro-
576 Imaging) equipped with an Airyscan 2 super-resolution module using a x60 oil-immersion
577 objective or by STED microscopy using an Axio Observer 7 (Carl Zeiss Micro-Imaging)
578 equipped with a STEDYCON module (Abberior) using a x100 oil-immersion objective.

579 For the study of HeLa *PML*^{L218Y}, stably expressing cells were fixed with 4%
580 paraformaldehyde and permeabilized with 0.1% Triton X-100. Slides were blocked with 2%
581 BSA in PBS, followed by incubation with anti-Flag antibodies (Sigma-Aldrich; Cat. n°F1804)
582 overnight at 4°C. Secondary antibodies (Abbkine; Cat. n°A23210) were incubated at room
583 temperature for 4 h. Slides were mounted using DAPI Fluoromount-G (Southern Biotech;
584 Cat. n°0100-20). The fluorescent signals were visualized under a Zeiss 510 confocal
585 microscope (Carl Zeiss Micro-Imaging).

586 **Live cell imaging and analysis of PML NBs**

587 All live-cell analysis were performed using glass-bottom culture dishes (IBIDI; Cat.
588 n°81156). For the analysis of NB formation *Pml*^{KO} cells were transduced with the culture
589 supernatant of Platinum-E cells transfected two days prior with a pMSCVpuro-GFP-PMLIII
590 vector. 1mL of anti-evaporation oil was added on top of the supernatant (IBIDI; Cat.
591 n°50051). The acquisition was performed on an Axio Observer video-microscope (Carl Zeiss
592 Micro-Imaging) equipped with a thermostatic chamber (37°C, 5% CO₂). Laser power and
593 exposure time were set at minimum levels to avoid photo-toxicity. Acquisitions were
594 performed every 15 minutes. PML NB formation was tracked in the same cells during the
595 entire experiment.

596 The quantification of PML NB nucleation/fusion/fission events was performed on
597 *Pml*^{KO} MEFs stably expressing GFP-PMLIII on a spinning disk confocal microscope (Nikon
598 Eclipse Ti, Nikon) equipped with a Coolsnap HQ2 high-sensitivity camera (Photometrics) and
599 a thermostatic chamber (37°C, 5% CO₂). Cells were imaged during two hours every 30
600 seconds. Quantification was performed using the FIJI software on maximum Z projections of
601 n=37 cells from four independent experiments. The magnitude of the effective viscosity of
602 the PML NBs was estimated by quantifying the time required for two NBs to relax in a
603 spherical structure during a fusion event as described before (66). The relaxation time during
604 a fusion event was quantified by measuring the long axis of the two condensates from the
605 beginning of the fusion and was plotted as a function of time for n=21 NBs from three
606 independent experiments. By computing the fusion time as a function of the diameter of the
607 resulting PML bodies (Supplementary Figure S1B) and by assuming that surface tension
608 drives the fusion process whereas viscosity tends to impede it, we determined that PML
609 bodies have an effective viscosity of about 10³ Pa.s. Analysis of PML NB distribution was
610 performed on confocal images of fixed cells using the FIJI software.

611 **Analysis by Fluorescence Recovery After Photobleaching (FRAP)**

612 FRAP was performed on *Pml*^{KO} MEFs stably expressing GFP-PMLIII, GFP-PML-RARA
613 or the indicated B2 mutants. 1µm regions of interest were used for GFP-PMLIII-expressing
614 cells and 2µm ROI were used for GFP-PML-RARA. Acquisitions were performed every 10
615 seconds using a spinning disk confocal microscope (Nikon Eclipse Ti, Nikon) equipped with a
616 Coolsnap HQ2 high-sensitivity camera (Photometrics) and a thermostatic chamber (37°C, 5%
617 CO₂) with a x60 oil-immersion objective. Three images were taken before photobleaching, 15
618 iterations were used to bleach the ROI and fluorescence recovery was followed every 10
619 seconds for 15-30 mins. On the graphs, only the data points pre-bleaching, immediately after

620 bleaching and every 2.5 mins are shown. Fluorescence recovery was analyzed using the FIJI
621 software. For each studied nucleus, the relative fluorescent intensity (RFI) was calculated as
622 previously described using an ImageJ plugin (67). Background correction was applied at
623 every time point and a double normalization was performed to account for global sample
624 bleaching. We assessed that PML recovery was independent of the size of the bleached area
625 by testing several sizes of photobleached areas, showing that interactions between PML
626 proteins at the shell have a predominant role over free diffusion. Then every RFI curve was
627 fitted to an $y=A*[1-\exp(-B/t)]$ model where y is the fluorescence intensity, A the plateau of
628 the intensity (mobile fraction), B the time in seconds and t the half-recovery time ($t_{1/2}$).

629 **Protein expression and purification from bacteria**

630 *Escherichia coli* Rosetta (DE3) cells (Novagen) were transformed with a pRSFDuet-1
631 vector (Novagen) containing the DNA sequence of human PML B2 domain fused to a MBP
632 tag. 0.2 mM IPTG was added into the culture to induce expression of the recombinant
633 proteins at 18 °C for 16 hours. Bacteria were harvested by centrifugation (5000 rpm, 8 min),
634 resuspended in a buffer containing 20 mM Tris-HCl pH8.0, 300 mM NaCl, 5% glycerol, 0.3
635 mM TCEP, 1 mM PMSF) and lysed using a cell disruptor (JNBIO). The lysate was loaded onto
636 a pre-equilibrated amylose resin column (NEB). The column was first washed with 5 column
637 volume of lysis buffer and MBP-B2 protein was eluted with a buffer containing 20 mM Tris-
638 HCl pH 8.0, 300 mM NaCl, 5% glycerol, 0.3 mM TCEP, 10 mM maltose. Proteins were
639 concentrated to 20 mg/mL and purified on a Superdex 200 increase gel filtration column
640 (Cytiva) (20 mM Tris-HCl pH 8.0, 200 mM NaCl, 0.3 mM TCEP). Purified MBP-B2 was
641 concentrated to 15 mg/mL for crystallization.

642 **Crystallization and structure determination**

643 Crystals of WT MBP-B2 were grown with 24-well plates using the hanging drop
644 vapor diffusion method by mixing 1.2 μ l protein (15 mg/mL) with 1.2 μ l crystallization buffer
645 containing 100 mM MES pH 6.5, 250 mM potassium acetate, 22% (w/v) PEG 3350. Crystals
646 grew to full size after incubation at 16°C for 1 week. MBP-B2 C213A and A216V mutant
647 proteins were crystallized in the same conditions. Before X-ray diffraction, crystals were cryo-
648 protected with the reservoir solution supplemented with 25% glycerol and were flash-cooled
649 into liquid nitrogen. Diffraction data were collected at Beamline station BL19U1 of Shanghai
650 Synchrotron Radiation Facility (SSRF, Shanghai, China), integrated and scaled using XDS and
651 the CCP4 program Pointless and Aimless (68-70). The structure of MBP-B2 was determined
652 by molecular replacement using the MBP structure from PDB 1ANF as an initial searching
653 model with Phaser (71). The structural model was built using Coot (72) and refined using
654 PHENIX (73). The structure of MBP-B2 C213A and A216V was determined using WT MBP-B2
655 structure as the initial search model. Figures were generated using PyMOL (The PyMOL
656 Molecular Graphics System, Version 2.0 Schrödinger, LLC). The statistics of the data
657 collection and refinement are shown in Supplementary Table S4. The B2 trimer model was
658 generated with Alphafold 2 (74). "Relevant crystallographic data collection and refinement
659 statistics are provided in Supplementary Table S4. Experimentally-determined 3D structures
660 can be found from the Protein Data Bank (PDB ID : 8J2P)"

661 **SEC-MALS analysis**

662 SEC-MALS were performed using a Superdex 200 increase column (Cytiva)
663 combined with multi-angle laser light scattering using a Wyatt HELEOS-II 18-angle
664 photometer coupled to a Wyatt Optilab rEX differential refractometer (Wyatt Technology
665 Corp). Experiments were carried out at room temperature with a protein concentration of
666 2.0 mg/mL and a flow rate of 0.5 mL/min in 20 mM Tris-HCl pH 8.0, 200 mM NaCl, 0.3 mM

667 TCEP. The data were analyzed using the ASTRA 6.1 software (Wyatt). The molecular mass
668 was determined across the protein elution peak.

669 **CRISPR/Cas9 knock-in mESCs and His pulldown**

670 *Pml*^{KO} cells were generated as described previously (21). To generate *Pml*^{L222G}
671 mESC, gRNA targeting mouse *Pml* (5'-G• CCG AGG CTG CGC CAA GCC TCT GTG TTG CAC ATG
672 CGC GCT CGG GGA CCG CAA CCA CAG CCA TCT CCA TTG CGA TAT TGG TG•A• G-3') and
673 recombinant Cas9 protein were synthesized from IDT to form Alt-R CRISPR/Cas9
674 ribonucleoprotein. mESCs were transiently transfected with Alt-R CRISPR/Cas9
675 ribonucleoprotein by using AmaxaTm mouse ES cell NucleofectorTm kit (Lonza; Cat n°VPH-
676 1001) and program number A-013 from the nucleofector 2b device (Lonza). After three days,
677 200 mESCs were spread on 150mm cell culture dishes and cultured until forming visible
678 colonies. After isolation and expansion, the DNA was extracted from these clones and
679 genotyping was performed using PCR primers: 5'-GGTTGTCAGACTTGGCTGTG-3' and 5'-
680 GCAGCTGGACTTTCTGGTTCT-3. Products were sequenced with primer: 5'-
681 ATCTCTTTGTAAGTGTCTGG-3' (Eurofins genomics). mESC were transduced using viral particles
682 produced by Platinum-E cells, as described above, after transfection with MSCV-IRES-GFP
683 constructs expressing His10-HA-SUMO2. His10-HA-SUMO2 conjugates were purified using
684 NiNTA agarose beads (Qiagen; Cat L30210) using Guanidium denaturing lysis as described
685 before (21).

686 **Mouse model generation**

687 *Pml*^{A220V} mice were obtained by CRISPR/Cas9 genome edition, performed on
688 BALB/cByJ zygotes, using TAKE methods (75). Briefly, three- to four-week-old BALB/cByJ
689 females were super-ovulated using CARD HyperOva (Cosmo bio, #KYD-010-EX) and human
690 Chorionic Gonadotropin, Sigma; #CG-10) and then mated with males (8-20 weeks) to get

691 zygotes. crRNA, TracrRNA, ssDNA and Cas9 nuclease were purchased from IDT and
692 electroporated (NEPA21; Sonidal) to introduce Pml point mutation encoding A220V
693 substitution using Pml target site: 5'-GTGTTGCACATGCGCGCTCC-3' and ssDNA donor
694 sequence:

695 5'CATCTACTGCCGAGGCTGCGCCAAGCCTCTGTGTTGCACATGCGTGCTCCTCGACCGCAACCACAG
696 CCATCTCCATTGCG-3'. Genotyping was performed using PCR primers: 5'-
697 GGTGTCAGACTTGCTGTG-3' and 5'-GCAGCTGGACTTTCTGGTTCT-3 and products were
698 sequenced with primer: 5'-ATCTCTTTGACTGTCTGG-3' (Eurofins genomics). This study has
699 been carried out in accordance with national (n° 2013-118) and European (n°2010/63/UE)
700 directives for animal experiments. Animals were handled according to the guidelines of
701 institutional animal care committees using protocols approved by the "Comité d'Ethique
702 Experimentation Animal Paris-Nord" (no. 121). Animals were housed at our animal facility
703 (UMS Saint-Louis US53/UAR2030, Institut de Recherche Saint-Louis, Paris, France) in
704 accordance with animal welfare and ethical guidelines (accreditation number B75-10-08).

705 ***In vivo* oxidative stress induction models**

706 For the transcriptomic study, an early oxidative stress model was used. A female mice
707 cohort (8-10 weeks) were treated with one intraperitoneal (IP) injections of 20% Carbon
708 tetrachloride CCl₄ (SIGMA; Cat n°289116) diluted in mineral oil (SIGMA; Cat n°M8410) or
709 one IP injection of mineral oil (2,5 µL/g, n=5 for each group). Mice were sacrificed 18h after
710 injections and livers were dissected as follows: left median lobes were stored in RNAlater
711 solution (Invitrogen; Cat n°AM7021) before RNA extraction, right median lobes were frozen
712 in tissue freezing medium (Leica Biosystems; Cat n°14020108926), right lobes were frozen in
713 liquid nitrogen for protein extraction, and left lobes were fixed in AFA fixative solution (VWR;
714 Cat n°11656713) for 24h and embedded in paraffin for histology staining.

715 To study a model of longer oxidative stress induction, liver fibrosis was triggered on a
716 female cohort by using 5 weeks treatment of 20% CCl₄, two IP injections per week (n=7
717 CCl₄-treated, n=3 oil-treated). Mice were sacrificed 48h after the last injection, and livers
718 were dissected as follows: right median lobes were frozen in tissue freezing medium and left
719 lobes were fixed in AFA fixative solution, embedded in paraffin. The protocol was approved
720 and performed in accordance with animal welfare and ethical guidelines (accreditation
721 number B75-10-08).

722 **Picro-Sirius Red Staining and Fibrosis quantification**

723 To assess the liver fibrosis, paraffin embedded tissue sections (6 μm) were
724 deparaffinized, rehydrated and stained during 1 hour in a 0,1% Picro-Sirius Red homemade
725 solution : Direct80 (SIGMA; Cat n°365548) diluted in an aqueous solution saturated in picric
726 acid. The stained liver sections were washed in acidified water, dehydrated in several
727 ethanol baths, cleared in SubX (Leica Biosystems; Cat n°3803670E) and mounted with a
728 permanent mounting medium. Each stained slide were scanned using the Zeiss AxioScan 7
729 (Carl Zeiss Micro-Imaging). The red collagen fibers stained by Picro-Sirius Red solution, were
730 quantified using an open source software, QuPath (76).

731 **RNA Extraction and Gene Chip Analysis**

732 Total RNA was extracted using TRIzol (Life Technologies, Grand Island, NY, USA)
733 according to the manufacturer's protocol. Triplicate samples were generated for each
734 genotype, from three *Pml*^{WT}, three *PML*^{KO}, and three *Pml*^{A220V} mice. MTA1.0 Affymetrix
735 Protocol was performed as following. RNA quantification and quality control was performed
736 using the HT RNA Reagent Kit (Perkin Elmer; Cat n°CLS960010,), the DNA 5KRNA/CZE
737 LabChip (Perkin Elmer; Cat n°760435) and the Caliper LabChip Microfluidics System (Perkin
738 Elmer; Cat n° GX1133N0432). One hundred nanogrammes of Total RNA was amplified,

739 labeled, and fragmented using GeneChip Plus Reagent Kit (ThermoFisher Scientific; Cat
740 n°902314). Each sample was hybridized onto GeneChip® Mouse Transcriptome Array 1.0
741 (ThermoFisher Scientific; Cat n°902514), washed, and stained using the GeneChip™
742 Hybridization, Wash, and Stain Kit (ThermoFisher Scientific; Cat n°900720) by using the
743 Affymetrix® Fluidics Station 450 (ThermoFisher Scientific; Cat n°60110150). Array Scanning
744 was performed with the Affymetrix® GeneChip Scanner 3000 7G (ThermoFisher Scientific,
745 Cat n°54714280), using the Command Console software (ThermoFisher Scientific) and then
746 analyzed using the Affymetrix® rma-sketch routine (Transcriptome Analysis Console (TAC)
747 software v.4.0.1, ThermoFisher Scientific). Raw microarray data (CEL files) were corrected for
748 background, \log_2 -transformed and normalized using the standard method RMA (robust
749 multi-array average) implemented in the oligo package (77). Quantile normalization was
750 then applied to mitigate the effects of technical variables using limma package (78) and
751 probe sets were annotated using mta10transcriptcluster.db package. A linear model fitted in
752 Limma package was performed to identify differential gene expression between Pml^{A220V}
753 versus Pml^{WT} or Pml^{KO} versus Pml^{WT} in basal conditions and after 18h of CCl4 treatment.
754 Differentially expressed genes were identified based on the adjusted p -value < 0.05 and
755 filtered with a fold change absolute value > 2 . Gene set enrichment analyses (GSEA) were
756 then performed to identify significant hallmark gene sets using the fgsea and msigdb
757 packages.

758 **Statistical Analysis**

759 Statistical tests performed with Graphpad prism are indicated in the figure legends.
760 Kruskal-Wallis test was used to determine the p -value and look for significant changes in
761 PML dynamics at NBs in Pml^{KO} fibroblasts stably expressing GFP-PML. All data are expressed

762 as mean \pm SD of technical or biological replicates as indicated. For all graphs, * P = 0.01-0.05,
763 ** P = 0.001-0.01, and *** P < 0.001.

764 **Data availability statement**

765 Experimentally-determined 3D structures can be found from the Protein Data Bank (PDB ID:
766 8J2P).

767 Sources for reagents and cells are indicated in Supplementary tables S2,S3.

768 Primary transcriptomic data are accessible on ArrayExpress (accession ID: E-MTAB-13183);

769 (For the reviewers : Login: pierre.bercier@college-de-france.fr; Pswd : nFjSz9JsA!cTTsD)

770 The data generated in this study are available upon request from the corresponding authors.

771

772 **REFERENCES**

773 1. Lallemand-Breitenbach V, de The H. PML nuclear bodies: from architecture to
774 function. *Curr Opin Cell Biol* **2018**;52:154-61 doi 10.1016/j.ceb.2018.03.011.

775 2. Hsu KS, Kao HY. PML: Regulation and multifaceted function beyond tumor
776 suppression. *Cell Biosci* **2018**;8:5 doi 10.1186/s13578-018-0204-8.

777 3. de The H, Pandolfi PP, Chen Z. Acute Promyelocytic Leukemia: A Paradigm for
778 Oncoprotein-Targeted Cure. *Cancer Cell* **2017**;32(5):552-60 doi 10.1016/j.ccell.2017.10.002.

779 4. Gurrieri C, Nafa K, Merghoub T, Bernardi R, Capodici P, Biondi A, *et al.* Mutations of
780 the PML tumor suppressor gene in acute promyelocytic leukemia. *Blood* **2004**;103(6):2358-
781 62 doi 10.1182/blood-2003-07-2200.

782 5. Koken MHM, Linares-Cruz G, Quignon F, Viron A, Chelbi-Alix MK, Sobczak-Thépot J, *et*
783 *al.* The PML growth-suppressor has an altered expression in human oncogenesis. *Oncogene*
784 **1995**;10:1315-24.

- 785 6. Mathews V, George B, Chendamarai E, Lakshmi KM, Desire S, Balasubramanian P, *et*
786 *al.* Single-agent arsenic trioxide in the treatment of newly diagnosed acute promyelocytic
787 leukemia: long-term follow-up data. *J Clin Oncol* **2010**;28(24):3866-71 doi [JCO.2010.28.5031](https://doi.org/10.1200/JCO.2010.28.5031)
788 [[pii](https://pubmed.ncbi.nlm.nih.gov/2010/1200/JCO.2010.28.5031/)] [10.1200/JCO.2010.28.5031](https://pubmed.ncbi.nlm.nih.gov/2010/1200/JCO.2010.28.5031/).
- 789 7. Mathews V, George B, Lakshmi KM, Viswabandya A, Bajel A, Balasubramanian P, *et*
790 *al.* Single-agent arsenic trioxide in the treatment of newly diagnosed acute promyelocytic
791 leukemia: durable remissions with minimal toxicity. *Blood* **2006**;107(7):2627-32 doi 2005-08-
792 3532 [[pii](https://pubmed.ncbi.nlm.nih.gov/2005/08/3532/)] [10.1182/blood-2005-08-3532](https://pubmed.ncbi.nlm.nih.gov/2005/08/3532/).
- 793 8. Jeanne M, Lallemand-Breitenbach V, Ferhi O, Koken M, Le Bras M, Duffort S, *et al.*
794 PML/RARA oxidation and arsenic binding initiate the antileukemia response of As2O3.
795 *Cancer Cell* **2010**;18(1):88-98 doi [S1535-6108\(10\)00241-2](https://doi.org/10.1016/j.ccr.2010.06.003) [[pii](https://pubmed.ncbi.nlm.nih.gov/2010/1016/j.ccr.2010.06.003/)] [10.1016/j.ccr.2010.06.003](https://pubmed.ncbi.nlm.nih.gov/2010/1016/j.ccr.2010.06.003/).
- 796 9. Zhang XW, Yan XJ, Zhou ZR, Yang FF, Wu ZY, Sun HB, *et al.* Arsenic trioxide controls
797 the fate of the PML-RARalpha oncoprotein by directly binding PML. *Science*
798 **2010**;328(5975):240-3 doi [10.1126/science.1183424](https://doi.org/10.1126/science.1183424).
- 799 10. Lallemand-Breitenbach V, Jeanne M, Benhenda S, Nasr R, Lei M, Peres L, *et al.* Arsenic
800 degrades PML or PML-RARalpha through a SUMO-triggered RNF4/ubiquitin-mediated
801 pathway. *Nat Cell Biol* **2008**;10(5):547-55 doi [ncb1717](https://doi.org/10.1038/ncb1717) [[pii](https://pubmed.ncbi.nlm.nih.gov/2008/1038/ncb1717/)] [10.1038/ncb1717](https://pubmed.ncbi.nlm.nih.gov/2008/1038/ncb1717/).
- 802 11. Banani SF, Lee HO, Hyman AA, Rosen MK. Biomolecular condensates: organizers of
803 cellular biochemistry. *Nat Rev Mol Cell Biol* **2017**;18(5):285-98 doi [10.1038/nrm.2017.7](https://doi.org/10.1038/nrm.2017.7).
- 804 12. Shin Y, Berry J, Pannucci N, Haataja MP, Toettcher JE, Brangwynne CP.
805 Spatiotemporal Control of Intracellular Phase Transitions Using Light-Activated optoDroplets.
806 *Cell* **2017**;168(1-2):159-71 e14 doi [10.1016/j.cell.2016.11.054](https://doi.org/10.1016/j.cell.2016.11.054).
- 807 13. Mehta S, Zhang J. Liquid-liquid phase separation drives cellular function and
808 dysfunction in cancer. *Nat Rev Cancer* **2022**;22(4):239-52 doi [10.1038/s41568-022-00444-7](https://doi.org/10.1038/s41568-022-00444-7).

- 809 14. Mann JR, Donnelly CJ. RNA modulates physiological and neuropathological protein
810 phase transitions. *Neuron* **2021**;109(17):2663-81 doi 10.1016/j.neuron.2021.06.023.
- 811 15. Ahn JH, Davis ES, Daugird TA, Zhao S, Quiroga IY, Uryu H, *et al.* Phase separation
812 drives aberrant chromatin looping and cancer development. *Nature* **2021**;595(7868):591-5
813 doi 10.1038/s41586-021-03662-5.
- 814 16. Chong S, Graham TGW, Dugast-Darzacq C, Dailey GM, Darzacq X, Tjian R. Tuning
815 levels of low-complexity domain interactions to modulate endogenous oncogenic
816 transcription. *Mol Cell* **2022**;82(11):2084-97 e5 doi 10.1016/j.molcel.2022.04.007.
- 817 17. Banani SF, Rice AM, Peeples WB, Lin Y, Jain S, Parker R, *et al.* Compositional Control
818 of Phase-Separated Cellular Bodies. *Cell* **2016**;166(3):651-63 doi 10.1016/j.cell.2016.06.010.
- 819 18. Sahin U, Ferhi O, Jeanne M, Benhenda S, Berthier C, Jollivet F, *et al.* Oxidative stress-
820 induced assembly of PML nuclear bodies controls sumoylation of partner proteins. *J Cell Biol*
821 **2014**;204(6):931-45 doi 10.1083/jcb.201305148.
- 822 19. Barroso-Gomila O, Trulsson F, Muratore V, Canosa I, Merino-Cacho L, Cortazar AR, *et*
823 *al.* Identification of proximal SUMO-dependent interactors using SUMO-ID. *Nat Commun*
824 **2021**;12(1):6671 doi 10.1038/s41467-021-26807-6.
- 825 20. Stadler M, Chelbi-Alix MK, Koken MHM, Venturini L, Lee C, Saïb A, *et al.*
826 Transcriptional induction of the PML growth suppressor gene by interferons is mediated
827 through an ISRE and a GAS element. *Oncogene* **1995**;11:2565-73.
- 828 21. Tessier S, Ferhi O, Geoffroy MC, Gonzalez-Prieto R, Canat A, Quentin S, *et al.*
829 Exploration of nuclear body-enhanced sumoylation reveals that PML represses 2-cell
830 features of embryonic stem cells. *Nat Commun* **2022**;13(1):5726 doi 10.1038/s41467-022-
831 33147-6.

- 832 22. Brangwynne CP, Eckmann CR, Courson DS, Rybarska A, Hoegge C, Gharakhani J, *et al.*
833 Germline P granules are liquid droplets that localize by controlled dissolution/condensation.
834 *Science* **2009**;324(5935):1729-32 doi 10.1126/science.1172046.
- 835 23. Brangwynne CP, Mitchison TJ, Hyman AA. Active liquid-like behavior of nucleoli
836 determines their size and shape in *Xenopus laevis* oocytes. *Proc Natl Acad Sci U S A*
837 **2011**;108(11):4334-9 doi 10.1073/pnas.1017150108.
- 838 24. Kim J, Han KY, Khanna N, Ha T, Belmont AS. Nuclear speckle fusion via long-range
839 directional motion regulates speckle morphology after transcriptional inhibition. *J Cell Sci*
840 **2019**;132(8) doi 10.1242/jcs.226563.
- 841 25. Weidtkamp-Peters S, Lenser T, Negorev D, Gerstner N, Hofmann TG, Schwanitz G, *et*
842 *al.* Dynamics of component exchange at PML nuclear bodies. *J Cell Sci* **2008**;121(Pt 16):2731-
843 43 doi jcs.031922 [pii] 10.1242/jcs.031922.
- 844 26. Geoffroy MC, Jaffray EG, Walker KJ, Hay RT. Arsenic-induced SUMO-dependent
845 recruitment of RNF4 into PML nuclear bodies. *Mol Biol Cell* **2010**;21(23):4227-39 doi
846 10.1091/mbc.E10-05-0449.
- 847 27. Daniel M-T, Koken M, Romagné O, Barbey S, Bazarbachi A, Stadler M, *et al.* PML
848 protein expression in hematopoietic and acute promyelocytic leukemia cells. *Blood*
849 **1993**;82:1858-67.
- 850 28. Echaniz-Laguna A, Benoild A, Vinzio S, Fornecker LM, Lannes B, Goulle JP, *et al.*
851 Mitochondrial myopathy caused by arsenic trioxide therapy. *Blood* **2012**;119(18):4272-4 doi
852 10.1182/blood-2011-10-385138.
- 853 29. Flora SJ. Arsenic-induced oxidative stress and its reversibility following combined
854 administration of N-acetylcysteine and meso 2,3- dimercaptosuccinic acid in rats. *Clin Exp*
855 *Pharmacol Physiol* **1999**;26(11):865-9.

- 856 30. Han MJ, Hao J, Christodoulatos C, Korfiatis GP, Wan LJ, Meng X. Direct evidence of
857 arsenic(III)-carbonate complexes obtained using electrochemical scanning tunneling
858 microscopy. *Anal Chem* **2007**;79(10):3615-22 doi 10.1021/ac062244t.
- 859 31. Reymond A, Meroni G, Fantozzi A, Merla G, Cairo S, Luzi L, *et al.* The tripartite motif
860 family identifies cell compartments. *Embo J* **2001**;20(9):2140-51.
- 861 32. Weerapana E, Wang C, Simon GM, Richter F, Khare S, Dillon MB, *et al.* Quantitative
862 reactivity profiling predicts functional cysteines in proteomes. *Nature* **2010**;468(7325):790-5
863 doi 10.1038/nature09472.
- 864 33. Wu HC, Rerolle D, Berthier C, Hleihel R, Sakamoto T, Quentin S, *et al.* Actinomycin D
865 Targets NPM1c-Primed Mitochondria to Restore PML-Driven Senescence in AML Therapy.
866 *Cancer Discov* **2021**;11(12):3198-213 doi 10.1158/2159-8290.CD-21-0177.
- 867 34. Lallemand-Breitenbach V, Zhu J, de Thé H. Promyelocytic leukemia, a unique model
868 to design treatments targeting oncogenes. *Médecine /Sciences* **2001**;17:14-22.
- 869 35. Goto E, Tomita A, Hayakawa F, Atsumi A, Kiyoi H, Naoe T. Missense mutations in
870 PML-RARA are critical for the lack of responsiveness to arsenic trioxide treatment. *Blood*
871 **2011**;118(6):1600-9 doi 10.1182/blood-2011-01-329433.
- 872 36. Zhu HH, Qin YZ, Huang XJ. Resistance to arsenic therapy in acute promyelocytic
873 leukemia. *N Engl J Med* **2014**;370(19):1864-6 doi 10.1056/NEJMc1316382.
- 874 37. Lehmann-Che J, Bally C, de Thé H. Resistance to therapy in acute promyelocytic
875 leukemia. *N Engl J Med* **2014**;371(12):1170-2 doi 10.1056/NEJMc1409040.
- 876 38. Iaccarino L, Ottone T, Divona M, Cicconi L, Cairoli R, Voso MT, *et al.* Mutations
877 affecting both the rearranged and the unrearranged PML alleles in refractory acute
878 promyelocytic leukaemia. *Br J Haematol* **2016**;172(6):909-13 doi 10.1111/bjh.13910.

- 879 39. Wagner JM, Roganowicz MD, Skorupka K, Alam SL, Christensen D, Doss G, *et al.*
880 Mechanism of B-box 2 domain-mediated higher-order assembly of the retroviral restriction
881 factor TRIM5alpha. *Elife* **2016**;5 doi 10.7554/eLife.16309.
- 882 40. Stoll GA, Oda SI, Chong ZS, Yu M, McLaughlin SH, Modis Y. Structure of KAP1 tripartite
883 motif identifies molecular interfaces required for retroelement silencing. *Proc Natl Acad Sci*
884 U S A **2019**;116(30):15042-51 doi 10.1073/pnas.1901318116.
- 885 41. Wang QQ, Zhou XY, Zhang YF, Bu N, Zhou J, Cao FL, *et al.* Methylated arsenic
886 metabolites bind to PML protein but do not induce cellular differentiation and PML-
887 RARalpha protein degradation. *Oncotarget* **2015**;6(28):25646-59 doi
888 10.18632/oncotarget.4662.
- 889 42. Muller S, Miller WH, Dejean A. Trivalent antimonials induce degradation of the PML-
890 RAR oncoprotein and reorganization of the promyelocytic leukemia nuclear bodies in acute
891 promyelocytic leukemia NB4 cells. *Blood* **1998**;92:4308-16.
- 892 43. Lallemand-Breitenbach V, Zhu J, Puvion F, Koken M, Honore N, Doubeikovsky A, *et al.*
893 Role of Promyelocytic Leukemia (PML) Sumolation in Nuclear Body Formation, 11S
894 Proteasome Recruitment, and As(2)O(3)-induced PML or PML/Retinoic Acid Receptor alpha
895 Degradation. *J Exp Med* **2001**;193(12):1361-72.
- 896 44. Koken MHM, Puvion-Dutilleul F, Guillemin MC, Viron A, Linares-Cruz G, Stuurman N,
897 *et al.* The t(15;17) translocation alters a nuclear body in a RA-reversible fashion. *EMBO J*
898 **1994**;13:1073-83.
- 899 45. de The H. Differentiation therapy revisited. *Nat Rev Cancer* **2018**;18(2):117-27 doi
900 10.1038/nrc.2017.103.

- 901 46. Niwa-Kawakita M, Ferhi O, Soilihi H, Le Bras M, Lallemand-Breitenbach V, de The H.
902 PML is a ROS sensor activating p53 upon oxidative stress. *J Exp Med* **2017**;214(11):3197-206
903 doi 10.1084/jem.20160301.
- 904 47. Gentric G, Kieffer Y, Mieulet V, Goundiam O, Bonneau C, Nemati F, *et al.* PML-
905 Regulated Mitochondrial Metabolism Enhances Chemosensitivity in Human Ovarian Cancers.
906 *Cell Metab* **2019**;29(1):156-73 e10 doi 10.1016/j.cmet.2018.09.002.
- 907 48. Alhazmi N, Pai CP, Albaqami A, Wang H, Zhao X, Chen M, *et al.* The promyelocytic
908 leukemia protein isoform PML1 is an oncoprotein and a direct target of the antioxidant
909 sulforaphane (SFN). *Biochim Biophys Acta Mol Cell Res* **2020**;1867(8):118707 doi
910 10.1016/j.bbamcr.2020.118707.
- 911 49. Guo L, Giasson BI, Glavis-Bloom A, Brewer MD, Shorter J, Gitler AD, *et al.* A cellular
912 system that degrades misfolded proteins and protects against neurodegeneration. *Mol Cell*
913 **2014**;55(1):15-30 doi 10.1016/j.molcel.2014.04.030.
- 914 50. Rerolle D, de The H. The PML hub: An emerging actor of leukemia therapies. *J Exp*
915 *Med* **2023**;220(8) doi 10.1084/jem.20221213.
- 916 51. Guo S, Cheng X, Lim JH, Liu Y, Kao HY. Control of antioxidative response by the tumor
917 suppressor protein PML through regulating Nrf2 activity. *Mol Biol Cell* 2014;25(16):2485-98
918 doi 10.1091/mbc.E13-11-0692.
- 919 52. Zhong S, Hu P, Ye TZ, Stan R, Ellis NA, Pandolfi PP. A role for PML and the nuclear
920 body in genomic stability. *Oncogene* **1999**;18:7941-7.
- 921 53. Krizhanovsky V, Yon M, Dickins RA, Hearn S, Simon J, Miething C, *et al.* Senescence of
922 activated stellate cells limits liver fibrosis. *Cell* **2008**;134(4):657-67 doi
923 10.1016/j.cell.2008.06.049.

- 924 54. Shen TH, Lin HK, Scaglioni PP, Yung TM, Pandolfi PP. The mechanisms of PML-nuclear
925 body formation. *Mol Cell* **2006**;24(3):331-9.
- 926 55. Shen S, Li XF, Cullen WR, Weinfeld M, Le XC. Arsenic binding to proteins. *Chem Rev*
927 **2013**;113(10):7769-92 doi 10.1021/cr300015c.
- 928 56. Zhang HN, Yang L, Ling JY, Czajkowsky DM, Wang JF, Zhang XW, *et al.* Systematic
929 identification of arsenic-binding proteins reveals that hexokinase-2 is inhibited by arsenic.
930 *Proc Natl Acad Sci U S A* **2015**;112(49):15084-9 doi 10.1073/pnas.1521316112.
- 931 57. Ablain J, Rice K, Soilhi H, de Reynies A, Minucci S, de Thé H. Activation of a
932 promyelocytic leukemia-tumor protein 53 axis underlies acute promyelocytic leukemia cure.
933 *Nat Med* **2014**;20(2):167-74 doi 10.1038/nm.3441.
- 934 58. Vitaliano-Prunier A, Halftermeyer J, Ablain J, de Reynies A, Peres L, Le Bras M, *et al.*
935 Clearance of PML/RARA-bound promoters suffice to initiate APL differentiation. *Blood*
936 **2014**;124(25):3772-80 doi 10.1182/blood-2014-03-561852.
- 937 59. Dagher T, Maslah N, Edmond V, Cassinat B, Vainchenker W, Giraudier S, *et al.*
938 JAK2V617F myeloproliferative neoplasm eradication by a novel interferon/arsenic therapy
939 involves PML. *J Exp Med* **2021**;218(2) doi 10.1084/jem.20201268.
- 940 60. Datta N, Chakraborty S, Basu M, Ghosh MK. Tumor Suppressors Having Oncogenic
941 Functions: The Double Agents. *Cells* **2020**;10(1) doi 10.3390/cells10010046.
- 942 61. Carracedo A, Weiss D, Leliaert AK, Bhasin M, de Boer VC, Laurent G, *et al.* A metabolic
943 pro-survival role for PML in breast cancer. *The Journal of clinical investigation*
944 **2012**;122(9):3088-100 doi 10.1172/JCI62129.
- 945 62. Zhu J, Chen Z, Lallemand-Breitenbach V, de Thé H. How acute promyelocytic
946 leukemia revived arsenic. *Nature Reviews on Cancer* **2002**;2:705-13.

- 947 63. de The H, Chen Z. Acute promyelocytic leukaemia: novel insights into the
948 mechanisms of cure. *Nat Rev Cancer* **2010**;10(11):775-83 doi [nrc2943](https://doi.org/10.1038/nrc2943) [pii]
949 [10.1038/nrc2943](https://doi.org/10.1038/nrc2943).
- 950 64. Madeira F, Pearce M, Tivey ARN, Basutkar P, Lee J, Edbali O, *et al*. Search and
951 sequence analysis tools services from EMBL-EBI in 2022. *Nucleic Acids Res*
952 **2022**;50(W1):W276-W9 doi [10.1093/nar/gkac240](https://doi.org/10.1093/nar/gkac240).
- 953 65. Zhu J, Zhou J, Peres L, Riaucoux F, Honore N, Kogan S, *et al*. A sumoylation site in
954 PML/RARA is essential for leukemic transformation. *Cancer Cell* **2005**;7(2):143-53.
- 955 66. Garcia-Jove Navarro M, Kashida S, Chouaib R, Souquere S, Pierron G, Weil D, *et al*.
956 RNA is a critical element for the sizing and the composition of phase-separated RNA-protein
957 condensates. *Nat Commun* **2019**;10(1):3230 doi [10.1038/s41467-019-11241-6](https://doi.org/10.1038/s41467-019-11241-6).
- 958 67. Sprague BL, Pego RL, Stavreva DA, McNally JG. Analysis of binding reactions by
959 fluorescence recovery after photobleaching. *Biophys J* **2004**;86(6):3473-95 doi
960 [10.1529/biophysj.103.026765](https://doi.org/10.1529/biophysj.103.026765).
- 961 68. Evans PR, Murshudov GN. How good are my data and what is the resolution? *Acta*
962 *Crystallogr D Biol Crystallogr* **2013**;69(Pt 7):1204-14 doi [10.1107/S0907444913000061](https://doi.org/10.1107/S0907444913000061).
- 963 69. Kabsch W. Xds. *Acta Crystallogr D Biol Crystallogr* **2010**;66(Pt 2):125-32 doi
964 [10.1107/S0907444909047337](https://doi.org/10.1107/S0907444909047337).
- 965 70. Winn MD, Ballard CC, Cowtan KD, Dodson EJ, Emsley P, Evans PR, *et al*. Overview of
966 the CCP4 suite and current developments. *Acta Crystallogr D Biol Crystallogr* **2011**;67(Pt
967 4):235-42 doi [10.1107/S0907444910045749](https://doi.org/10.1107/S0907444910045749).
- 968 71. McCoy AJ, Grosse-Kunstleve RW, Adams PD, Winn MD, Storoni LC, Read RJ. Phaser
969 crystallographic software. *J Appl Crystallogr* **2007**;40(Pt 4):658-74 doi
970 [10.1107/S0021889807021206](https://doi.org/10.1107/S0021889807021206).

971 72. Emsley P, Cowtan K. Coot: model-building tools for molecular graphics. *Acta*
972 *Crystallogr D Biol Crystallogr* **2004**;60(Pt 12 Pt 1):2126-32 doi 10.1107/S0907444904019158.

973 73. Liebschner D, Afonine PV, Baker ML, Bunkoczi G, Chen VB, Croll TI, *et al.*
974 Macromolecular structure determination using X-rays, neutrons and electrons: recent
975 developments in Phenix. *Acta Crystallogr D Struct Biol* **2019**;75(Pt 10):861-77 doi
976 10.1107/S2059798319011471.

977 74. Jumper J, Evans R, Pritzel A, Green T, Figurnov M, Ronneberger O, *et al.* Highly
978 accurate protein structure prediction with AlphaFold. *Nature* **2021**;596(7873):583-9 doi
979 10.1038/s41586-021-03819-2.

980 75. Hashimoto M, Takemoto T. Electroporation enables the efficient mRNA delivery into
981 the mouse zygotes and facilitates CRISPR/Cas9-based genome editing. *Sci Rep* **2015**;5:11315
982 doi 10.1038/srep11315.

983 76. Bankhead P, Loughrey MB, Fernandez JA, Dombrowski Y, McArt DG, Dunne PD, *et al.*
984 QuPath: Open source software for digital pathology image analysis. *Sci Rep* **2017**;7(1):16878
985 doi 10.1038/s41598-017-17204-5.

986 77. Carvalho BS, Irizarry RA. A framework for oligonucleotide microarray preprocessing.
987 *Bioinformatics* **2010**;26(19):2363-7 doi 10.1093/bioinformatics/btq431.

988 78. Ritchie ME, Phipson B, Wu D, Hu Y, Law CW, Shi W, *et al.* limma powers differential
989 expression analyses for RNA-sequencing and microarray studies. *Nucleic Acids Res*
990 **2015**;43(7):e47 doi 10.1093/nar/gkv007.

991

992 **FIGURE LEGENDS**

993 **Fig. 1. PML NBs display hallmarks of LLPS and switch to gel-like features upon ATO**
994 **exposure**

995 **A**, STED analysis uncovers the typical spherical core-shell PML NB. Scale bar: 1 μ m. **B**, Time-
996 lapse analysis of PML NB apparition upon GFP-PML expression in *Pml*^{-/-} MEFs. The white
997 circle indicates the nucleus. Representative data from three independent experiments. Scale
998 bar: 5 μ m. **C**, PML NBs undergo fusion with spherical relaxation, similar to liquid-like droplets.
999 Representative time-lapse of PML NB fusion (left) and quantification of effective viscosity
1000 (right). Mean values \pm SD of n=21 fusion events in independent cells from three independent
1001 experiments. Scale bar: 1 μ m. **D**, Quantification of PML NBs nucleation, fusion and fission
1002 events over one hour. Mean value \pm SD of n=37 cells from five independent experiments. **E**,
1003 FRAP analyses of GFP-PML^{WT} dynamics at NBs in control or ATO-treated MEFs (1 μ M, 30min).
1004 Mean value \pm SD. NB assessed Ctrl: n=36, ATO: n=28, from at least five independent
1005 experiments. **F**, Confocal analysis of PML NBs in GFP-PML^{WT} or GFP-PML-RARA^{WT} MEFs
1006 treated with 1 μ M of ATO for 1h. Scale bar: 5 μ m. **G**, STED analysis demonstrating incomplete
1007 PML NB fusion upon ATO. Scale bar: 1 μ m. **H**, Comparison between GFP-PML^{WT} and GFP-
1008 PML-RARA^{WT} dynamics at NBs by FRAP. ATO treatment (1 μ M, 30min) induces a liquid- to gel-
1009 like transition of GFP-PML-RARA WT. Mean value \pm SD. NBs assessed PML: n=36, PML-RARA:
1010 n=20, PML-RARA+ATO: n=37, from at least five independent experiments.

1011

1012 **Fig. 2. PML NB assembly depends on C213 in B2 zinc finger domain, but not on C389-**
1013 **mediated inter-molecular disulfide bonds**

1014 **A**, Confocal analysis of PML NB formation following cysteine alkylation with NEM (N-ethyl-
1015 maleimide, 10 μ M, 1h) or ATO (1 μ M, 1h) used alone or sequentially in GFP-PML^{WT} MEFs.

1016 Scale bar: 5 μ m. **B**, Western blot analysis (non-reducing conditions) of PML disulfide bond
 1017 formation in MEFs expressing HA-PML^{WT} or PML cysteine mutants, treated or not with ATO
 1018 (10 μ M, 1h) or H₂O₂ (500 μ M, 1h). Brackets: SUMO-conjugated and intermolecular disulfide-
 1019 bound PML. Blue arrowheads: intermolecular disulfide-bound PML. Molecular weight (kDa).
 1020 **C**, Confocal analysis of PML NBs upon ATO (1 μ M, 1h) or H₂O₂ (500 μ M, 1h) exposure in HA-
 1021 PML^{WT}- or cysteine mutant-expressing MEFs. Arrow: single NB in HA-PML^{C213A}-expressing
 1022 MEFs. Scale bar: 5 μ m.

1023

1024 **Fig. 3. Uncovering PML B2 structure**

1025 **A**, Conservation of PML B2 box through evolution. Top part: putative position of the two zinc
 1026 fingers intertwined in a cross-brace. Bold: amino acids implicated in putative zinc
 1027 coordination. The additional cysteine in position 213 is highlighted in blue. Predicted
 1028 secondary structures of PML B-box-2 are depicted, arrow: beta-sheet; loop: α 1-helix; Stars:
 1029 evolutionary conserved amino acids (bold: identical, custom: 1/6 variation only). The highly
 1030 conserved α helix is boxed in blue. Bottom part: PML-RARA mutations from therapy-
 1031 resistant APL patients. **B**, Crystal structure of PML B2 monomer shown in a cartoon
 1032 representation. PML B2 folds around two zinc fingers organized in a cross-brace. The C3H1
 1033 zinc coordination leaves the C213 free. α 1-helix (C213 to L218) exposes C213 towards the
 1034 outside of the structure. Spheres: zinc atoms, blue bold font: C213. **C**, (Left) Composite omit
 1035 map contoured at 2 σ of a segment from PML B2 near zinc finger 1 at 2.1 \AA . C213 appears as
 1036 a free cysteine (blue). (Right) Composite omit map contoured at 2 σ of a segment from PML
 1037 B2 near Zinc finger 2 at 2.1 \AA . C227, not D219, coordinates Zn²⁺. Cyan spheres, zinc atoms.

1038

1039 **Fig. 4. PML B2 α 1-helix controls PML assembly and dynamics**

1040 **A**, Representative PML NB formation in MEFs expressing PML B2 mutants in Zn²⁺-
 1041 coordinating cysteines or α 1-helix (underlined in blue) residues. Scale bar: 5 μ m. **B**, FRAP
 1042 analyses of GFP-PML dynamics at NBs in WT- or mutant-expressing MEFs. Mean value \pm SD.
 1043 R.F.I.: relative fluorescence intensity. NBs assessed PML^{WT}: n=36, PML^{C189S}: n=25, PML^{C212S}:
 1044 n=42, PML^{C213S}: n=24, PML^{L218G}: n=20, from at least five independent experiments. **C**, Plot
 1045 representation of **B**, with half recovery time (left) and immobile fraction (right) of PML
 1046 mutants harboring mutations on the α 1 -helix or zinc finger. Each dot represents an
 1047 individual NB. Median \pm 95% confidence interval, statistical significance by comparison with
 1048 GFP-PML, Kruskal-Wallis test. *** P \leq 0.001 are displayed. P-value for Zn-finger mutants,
 1049 C189S=0,0097, C212S=0,0115, C213S=0,028. **D**, Superposition of PML B2 crystal structure
 1050 (cyan) with that of PML^{C213A/A216V} mutant (orange) demonstrates absence of misfolding.

1051

1052 **Fig. 5. PML B2 mediates PML trimerization and is required for biological functions**

1053 **A**, Modelling of a PML B2 trimer. B2 monomers are colored in green, grey and pink.
 1054 Exponents refer to affiliation to a specific monomer. **B**, Close-up view of the PML B2 trimer
 1055 model depicting hydrophobic interactions between the α 1-helices. Residues involved in
 1056 these hydrophobic interactions are shown in blue, linked by dashed lines. Distance between
 1057 these key hydrophobic residues are in Å. **C**, SEC-MALS analysis showing a mix of monomeric,
 1058 dimeric and trimeric PML B2 (left). The C213A mutant shifts towards monomeric and dimeric
 1059 states (right). MBP-B2 MW: 46.2 kDa. **D**, Representative PML NB formation in PML B2
 1060 mutants predicted to impair trimerization expressed in MEFs. Scale bar: 5 μ m. **E**, GFP-
 1061 PML^{L218F} yields filaments (left). Scale bar: 5 μ m. FRAP analysis of the exchange rates of GFP-
 1062 PML^{L218F} mutant compared to GFP-PML (right). Mean value \pm SD. NBs assessed WT: n=36,
 1063 PML L218F: n=24, from at least five independent experiments.

1064

1065 **Fig. 6. ATO binding to B2 trimer is responsible for ATO-induced phase transition**

1066 **A**, Modelling of PML B2 trimer around an arsenic atom. The key C213 residue are indicated
1067 in blue and the arsenic atom is shown as an orange sphere. The predicted distance between
1068 the arsenic atom and C213, represented by the dashed line is 2.7 Å. **B**, FRAP analyses of GFP-
1069 PML dynamics at NBs in untreated cells or cells treated with trivalent metalloid oxides: ATO
1070 (1µM, 30min) or STO (1µM, 30min) or divalent arsenic (MMA, 1µM, 30min). Mean value ±
1071 SD., assessed NBs Ctrl: n=36, MMA: n=21, ATO: n=28, STO: n=33, from at least 5
1072 independent experiments. **C**, Representative confocal analyses of PML NB formation in *Pml*^{-/-}
1073 MEFs stably expressing GFP-PML B2 mutants, +/- ATO (1µM, 1h). Scale bar: 5µm. **D**, FRAP
1074 analyses of GFP-PML mutant-expressing MEFs treated or not with ATO (1µM, 30min). Mean
1075 value ± SD. NBs assessed PML^{C212S} Ctrl: n=42, PML^{C212S} ATO: n=28, PML^{C213S} Ctrl: n=24,
1076 PML^{C213S} ATO: n=27, PML^{L218G} Ctrl: n=20, PML^{L218G} ATO: n=26, PML^{A216G} Ctrl: n=40, PML^{A216G}
1077 ATO: n=28, PML^{A216V} Ctrl: n=43, PML^{A216V} ATO: n=43, PML^{C213V} Ctrl: n=32, PML^{C213V} ATO:
1078 n=31, from at least 5 independent experiments. **E**, Representative images of red fluorescent
1079 arsenic (ReAsH) localization to NBs in GFP-PML or mutant MEFs. Scale bar: 1µm. **F**,
1080 Representative PML NB formation in PML C213 mutant-expressing MEFs. Scale bar: 5µm. **G**,
1081 Confocal analysis of PML NB formation following cysteine alkylation with NEM (N-ethyl-
1082 maleimide 10µM, 1h) in GFP-PML or PML^{C213V} MEFs. Scale bar: 5µm. **H**, Western blot analysis
1083 of basal PML sumoylation in GFP-PML^{WT}- or mutant-expressing MEFs. **I**, Western blot
1084 analysis of PML sumoylation in GFP-PML^{WT} or mutant MEFs treated or not with ATO (1µM,
1085 1h). **J**, Confocal analysis of PML and Sp100 localization in GFP-PML- or C213 mutant-
1086 expressing MEFs treated or not with ATO (1µM, 1h). Scale bar: 5µm. **K**, Pulldown of HIS₁₀-
1087 SUMO₂ conjugates from *Pml*^{WT} or *Pml*^{L222G} mESCs treated or not with ATO (1µM, 30min).

1088 ATO-treated non-transduced *Pml*^{WT} mESCs are shown as controls. Western blot with anti-
1089 SUMO_{2/3} (left), anti-mPML (right, top) or anti-KAP1 antibodies (right, bottom). Sumoylated
1090 species are indicated. Representative data of n=3 independent experiments.

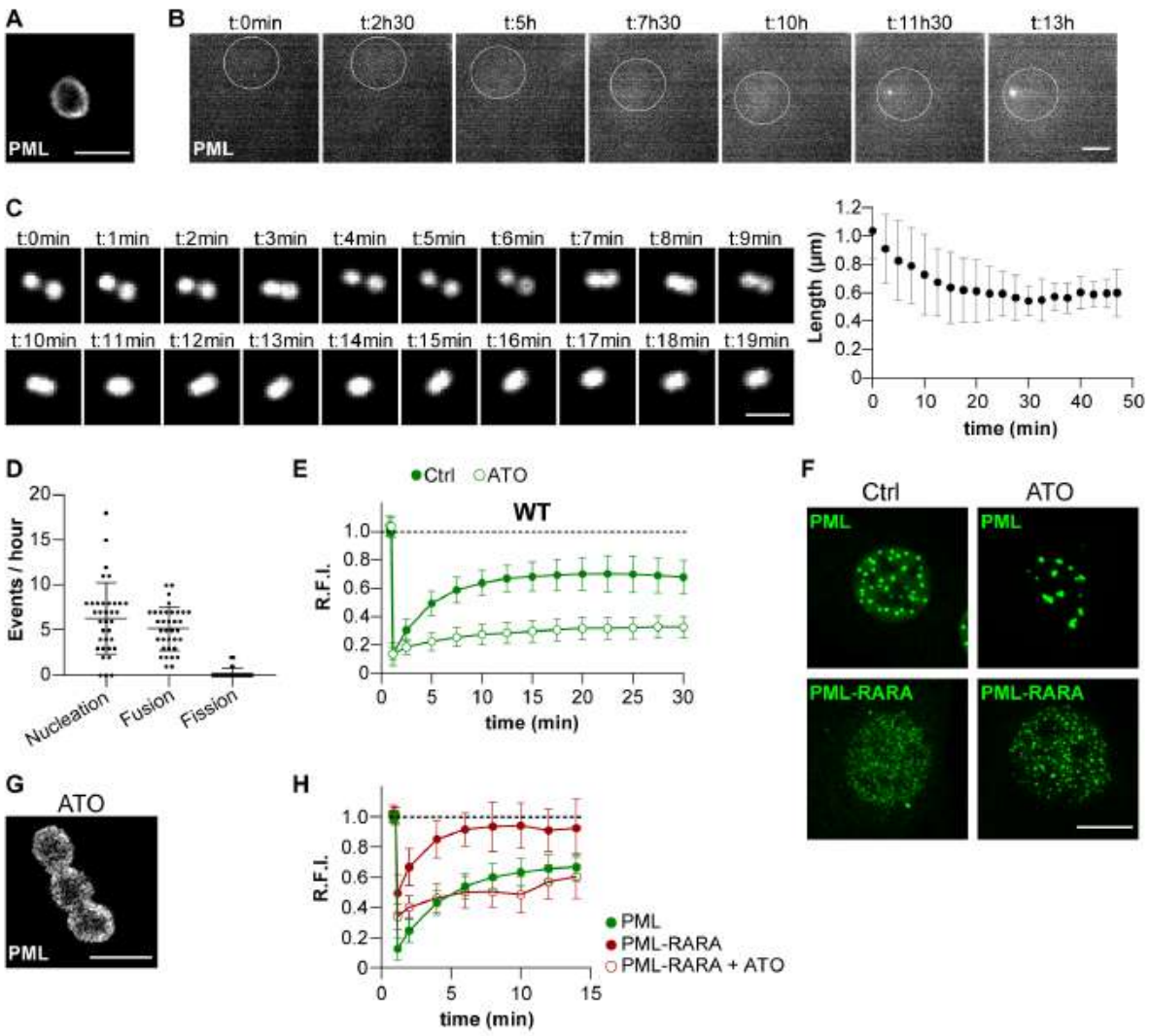
1091

1092 **Fig. 7. PML-RARA ATO-sensitivity requires C213 and B2 controls *in vivo* responses to ROS**

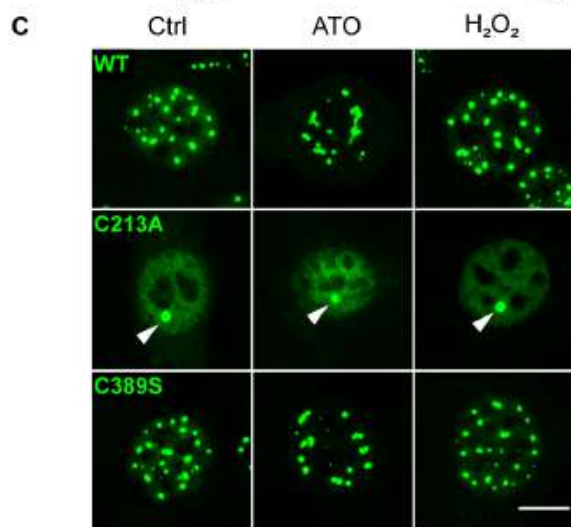
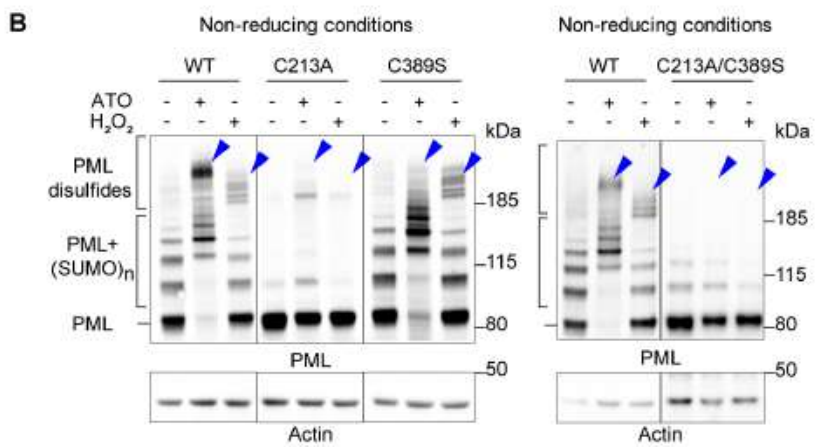
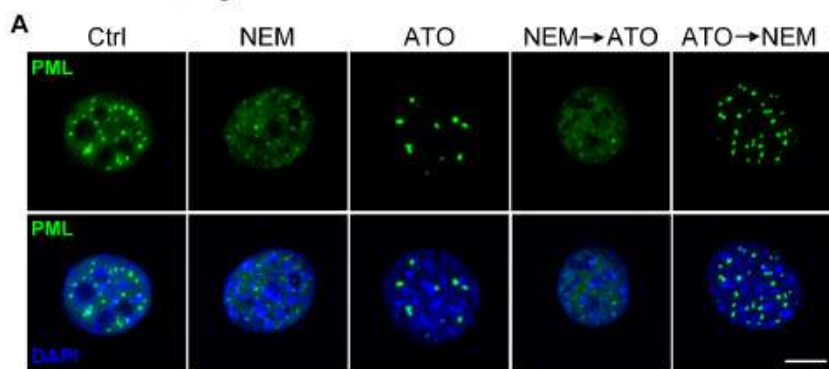
1093 **A**, Confocal analysis of *Pml*^{+/+} MEFs stably expressing human PML-RARA or its B2 mutants
1094 treated or not with ATO (1μM, 6h). Scale bar: 5μm. Different display settings for each
1095 genotype. **B**, Western blot analysis of PML-RARA sumoylation in Lin⁻ hematopoietic
1096 progenitors expressing PML-RARA or the indicated mutants, treated or not with ATO (1μM,
1097 1h). Representative data from three independent experiments. **C**, FRAP analysis of GFP-PML-
1098 RARA dynamics at NBs in GFP-PML-RARA^{WT}- or GFP-PML-RARA^{C213V}-expressing *Pml*^{-/-} MEFs
1099 treated or not with ATO (1μM, 30min). Mean value ± SD. NBs assessed PML-RARA^{WT}: n=20,
1100 PML-RARA^{WT}+ATO: n=37, PML-RARA^{C213V}: n=42, PML-RARA^{C213V}+ATO: n=25, from at least 5
1101 independent experiments. **D**, FRAP analysis of GFP-PML dynamics at NBs in MEFs treated or
1102 not with H₂O₂ (30min). Mean value ± SD. NB assessed PML: n= 35, H₂O₂ 100μM: n=27, H₂O₂
1103 500μM: n=32, from at least 5 independent experiments. **E**, Same as **D** with GFP-PML^{C213V}.
1104 Mean value ± SD. NB assessed PML^{C213V}: n= 32, H₂O₂ 100μM: n=24, H₂O₂ 500μM: n=22, from
1105 at least 5 independent experiments. **F**, Box plot representing γH2AX dots counts assessed by
1106 immunofluorescence on liver tissues from three untreated mice. *Pml*^{WT}: n=633, *PML*^{KO}:
1107 n=527, *Pml*^{A220V}: n=333. *** P ≤ 0.001, unpaired t-test. **G**, GSEA analysis of differentially
1108 expressed genes from liver samples from untreated *Pml* or *Pml*^{A220V} (equivalent of human
1109 *PML*^{A216V}) mice. Key pathways are boxed. Livers from n=3 *Pml* or *Pml*^{A220V} mice. **H**, GSEA of
1110 differentially expressed genes in liver samples from *Pml* or *Pml*^{A220V} in comparison to WT
1111 after a 18h CCl₄ treatment. Key pathways are boxed. Livers from n=3 mice of each genotype.

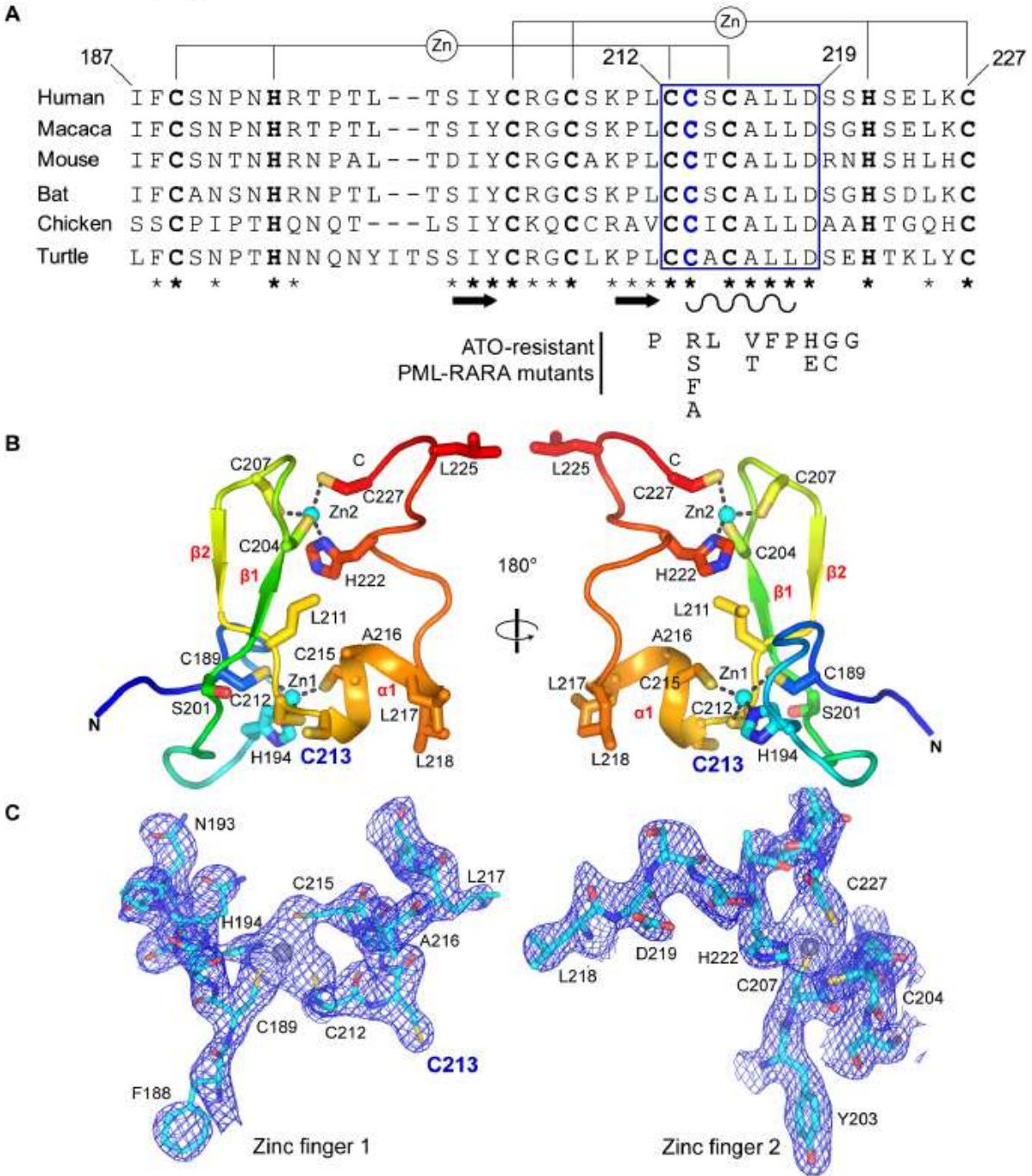
1112 **I**, Liver fibrosis following a 5 weeks CCl₄ treatment detected by Picro-Sirius Red staining (left).
1113 Quantification of the fibrotic areas (right). Livers from n=7 *Pml*, *Pml*^{KO} or *Pml*^{A220V} mice. Scale
1114 bar: 400μm. ** P ≤ 0.01, Mann-Whitney test. **J**, Model of PML NB liquid to gel-like transition
1115 controlled by the C213-containing B2 α1 helix hijacked by ATO. Hydrophobic-mediated
1116 trimerization of PML B2 (grey disk), regroups the three C213 in the center of the structure.
1117 The latter is impaired in α-helix mutants. In the physiological states, this C213 triad behaves
1118 as a rheostat depending on their oxidation state (asterisks), fine-tuning the interaction
1119 within the trimer (light and dark grey disk). Arsenic binding crosslinks these cysteines,
1120 highjacking the ROS-rheostat to yield polymerization-induced gel-like transition.

Bercier et al., Figure 1

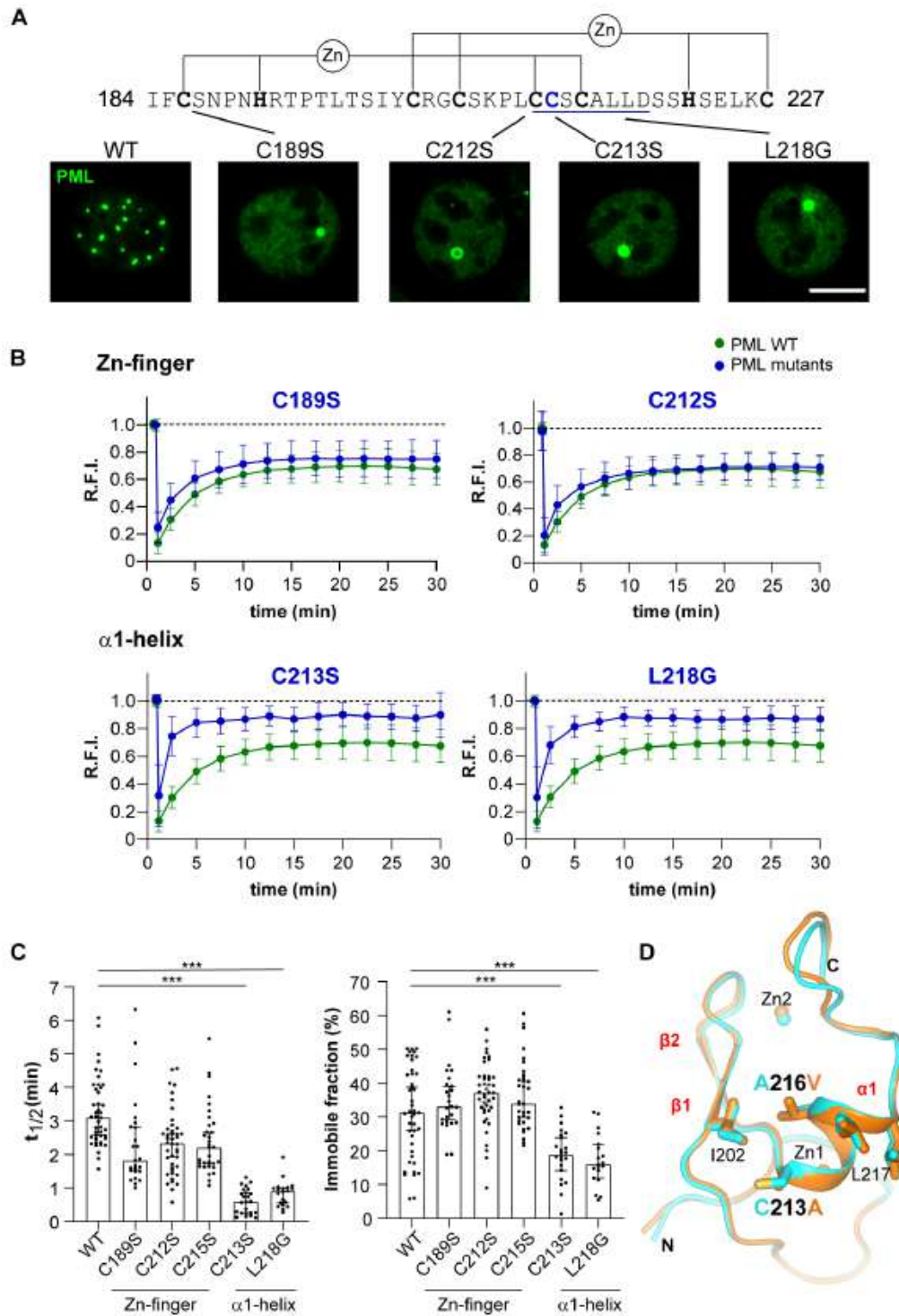


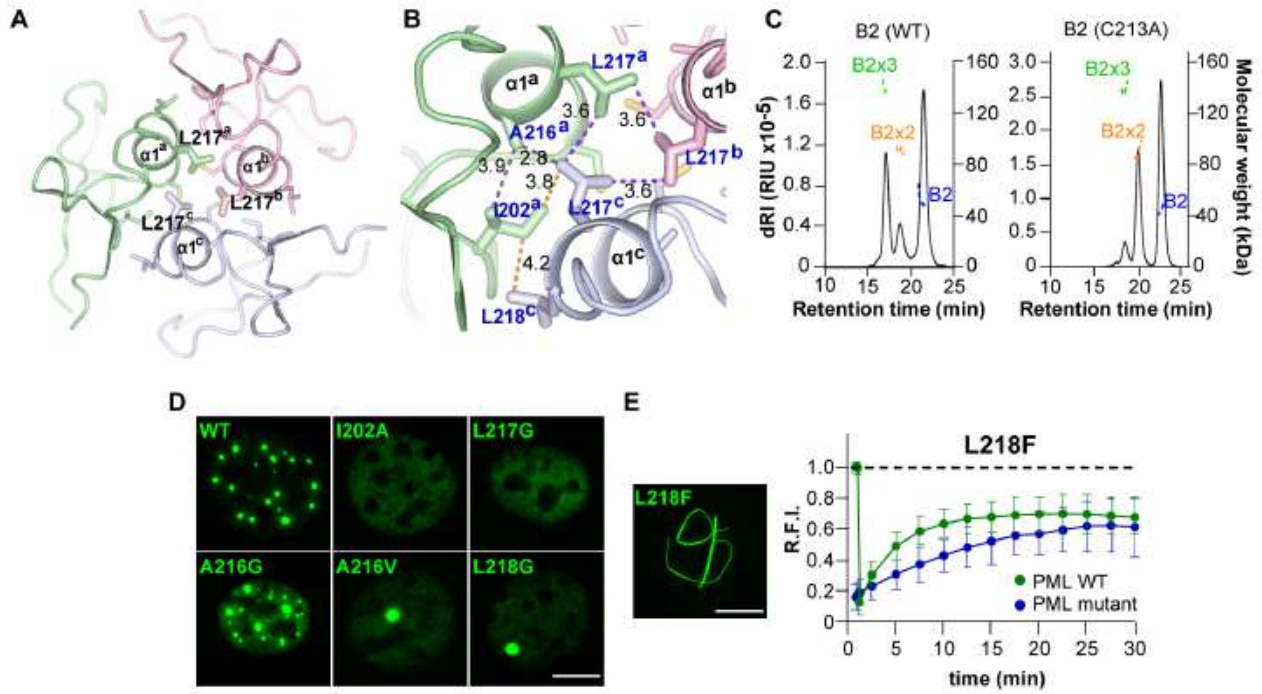
Bercier et al., Figure 2



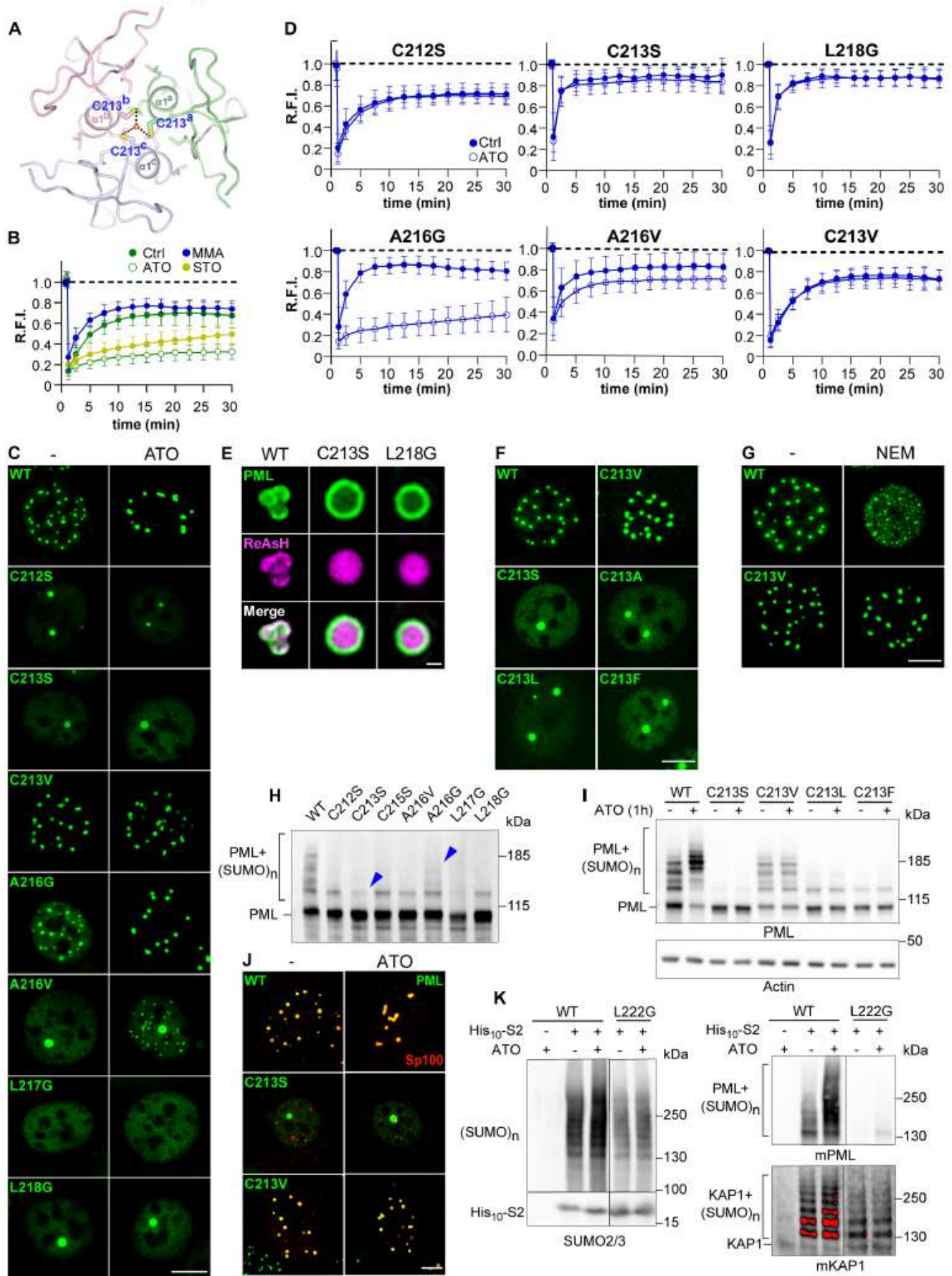


Bercier et al., Figure 4





Bercier et al., Figure 6



Bercier et al., Figure 7

